# On an objective, geometrically exact coupling element for a director-based multi-body finite element framework

David Märtins[1*], Daniel Schuster[1], Christian Hente[1], Cristian Guillermo Gebhardt[2], Raimund Rolfes[1]

[1]Leibniz Universität Hannover, Institute of Structural Analysis, ForWind, Appelstr. 9A, Hannover, 30167, Germany.
[2]University of Bergen, Bergen Offshore Wind Centre (BOW), Allégaten 70, Bergen, 5007, Norway.

*Corresponding author(s). E-mail(s): d.maertins@isd.uni-hannover.de ;
Contributing authors: d.schuster@isd.uni-hannover.de;
c.hente@isd.uni-hannover.de; cristian.gebhardt@uib.no;
r.rolfes@isd.uni-hannover.de;

**Abstract**

In multi-body systems, flexible components as well as couplings between them can be subject to large displacements and rotations. This contribution presents a general objective and geometrically exact node-to-node coupling element pursuing two innovations. Firstly, the coupling element represents a consistent contribution to an existing nonlinear mechanical framework. The coupling element intends to preserve its attributes of objectivity, path-independence, and adherence to the energy-conserving or energy-dissipative time integration method. Secondly, besides elasticity also inertia and damping properties are considered. For this purpose, a director-based formulation is employed within a total Lagrangian description. The avoidance of an angle-based representation, along with the additive update of state variables, results not only in path-independence but also in the avoidance of accumulating errors during extended simulations. An objective deformation measure is chosen based on the Green-Lagrange strain tensor. The inertia forces are considered by an arbitrarily shaped continuum located at the centre of the coupled nodes. Damping is considered by two different objective first order dissipation functions, which further ensure energy conservation or dissipation. We successfully demonstrate the coupling element within the mechanical framework on exemplary applications. Firstly, the geometrically exact behaviour

is shown compared to a linear deformation measure. Secondly, we numerically indicate the path-independence of the formulation. The dynamic behaviour is demonstrated in a transient analysis of a damped structure. Finally, the modal analysis of a wind turbine shows the application of the coupling element to model the soil-structure interaction.

**Keywords:** director-based kinematics, node-to-node coupling element, objectivity, geometrically exact deformation

# 1 Introduction

Flexible couplings between components in multi-body systems (MBSs) and structural systems can exhibit complex mechanical behaviour. The investigation of the detailed properties is a challenging task, necessitating sophisticated models or experiments. To achieve a balance between computational efficiency and accurate global behaviour approximation, the properties derived from detailed investigations can be incorporated into a coupling element. This can then be used to model MBS and structural systems. Especially when examining the nonlinear behaviour of mechanical models, it is crucial to also consider the geometrically nonlinear characteristics of its flexible couplings.
The motivation of this work is twofold. First, there is a need for a mechanical framework that can represent the nonlinear behaviour of structures. Second, the development of a general coupling element that equally models the geometric nonlinearity of connections without violating the consistency of the mechanical framework is necessary.
Geometric nonlinearities of complex mechanical systems consisting of slender structures can be modelled with appropriate nonlinear MBS. Such structures are for example slender and elastic aircraft wings, in which the occurring geometrical nonlinearity significantly affects the dynamic behaviour of the wing and thus the aircraft itself [1]. Another example is provided by energy converter turbines, in which turbine blades are being developed to be ever more slender due to increasing rotor sizes. Here, nonlinear geometric behaviour also has to be taken into account [2].
Moreover, couplings in these MBS can undergo large displacements and rotations, as well. To model their mechanical behaviour, geometrically nonlinearities again have to be considered. An example of couplings undergoing nonlinear geometrical deformation are adhesive lap-joints discussed by Andruet et al. [3]. These are subject to important geometric nonlinear effects due to eccentrically applied forces. Dispersyn et al. [4] investigate adhesive point fixings in structural glass facades, considering nonlinear geometric deformations and material nonlinearities. Similarly, in [5], a study of adhesively bonded composites and their thermal effects reveals that small strains and large displacements accurately represent the joint behaviour. Geometric nonlinearities also arise in the deformation of rubber bushings in automotive suspensions, as outlined in [6]. In MBS frameworks that analyse structural behaviour, these examples can be simplified into a coupling element with the appropriate properties.

In recent decades, MBS approaches were developed to consider nonlinear mechanical behaviour. The commonly used wind-turbine-specific codes [7–9] use angle-based geometrically exact beams to model slender components. This formulation, in combination with an updated Lagrangian description, does not maintain objectivity and path-independence. Borri et al. [10] present an invariant-preserving approach that maintains objectivity. This consists of rigid bodies, geometrically exact beams, shell elements and kinematic joints, and is formulated angle-based. Betsch et al. [11] and Romero et al. [12] introduce director-based geometrically exact beam formulations in a total Lagrangian description. Their formulations are objective and preserve the total energy of the system. Furthermore, the director-based formulation, in combination with additive updating of the rotation, leads to path-independence. Gebhardt et al. developed an MBS formulation, consisting of the three canonical models' rigid bodies, geometrically exact beams, and solid-degenerate shells [13–18]. Also, director-based kinematics in a total Lagrangian formulation are used to maintain objectivity and path-independence. The total energy of a mechanical system is preserved or dissipated using a time integration scheme, based on the midpoint rule and the *average-vector-field* method [19]. Singularities that might occur in the stiffness matrices formulated in [11] and [12] are avoided, allowing buckling analyses [20]. The presented coupling element is developed as a consistent contribution to this mechanical MBS framework. Coupling elements are implemented in commonly used MBSs and finite element (FE) codes. For instance, the well-established FE code ABAQUS [21] allows the use of linear translational and rotational spring elements (**SPRING*, **JOINTC*) to model node-to-node connections or to couple one node with the surrounding environment. Similarly, the multi-body dynamics software MSC ADAMS [22] provides integration options for *BUSHING* and *FIELD* elements, which calculate forces and moments on connected nodes based on a linear deformation measure. These coupling elements assume small deformations.

To address the limitations of linear deformation measures and enable the modeling of large displacements and rotations, Masarati and Morandini [23] developed a formulation that represents constitutive relations for lumped deformable components experiencing finite deformations. They found that nonlinear constitutive laws must be considered when strains are not small. However, large relative displacements and geometric nonlinear behaviour do not necessarily imply large strains. Bauchau [24] introduces a family of finite deformation measures suitable for characterising moderate deformations of flexible joints using angle-based kinematics. He demonstrates that combining tensorial deformation measures with linear constitutive laws accurately predict moderate deformations. An extensive derivation of an objective angle-based formulation is presented.

The newly developed coupling element described in this paper has the following two main innovations. First, the coupling element is a consistent extension of the presented mechanical MBS and FE framework. It is objective under rigid body motion, maintains path-independence and preserves linear and angular momentum as well as the total energy of the overall system. Fully nonlinear static and dynamic analyses can be carried out. Second, the element considers mass and damping without compromising

the desired properties. To the best of our knowledge, there is no literature on a general coupling element that considers elasticity, mass and damping in a single element. Masses that cause inertia forces are modelled as an arbitrary continuum between the nodes concerned. The objective strain/stress-dependent damping formulation derived by Armero and Romero [25] and Gebhardt et al. [19] is introduced. Additionally, we demonstrate the possibility of using dissipation functions tailored to specific physical problems, such as obtaining a strain-rate/stress-rate dependent damping.
The work is structured as follows: in section 2 the main ideas behind the mechanical framework are presented. The equations incorporating the stiffness, mass, and damping properties of the coupling element are derived in section 3. In section 4, application examples are given to illustrate the behaviour of the coupling element. Finally, a summary of the work together with limiting aspects and an outlook on future work is given in section 5.

# 2 Mechanical framework

The general coupling element presented in this work is a consistent extension of the mechanical MBS framework developed by Gebhardt et al. [13–20]. The framework uses a mixed displacement-velocity-strain-based formulation and director-based kinematics in a total Lagrangian description. It comprises three canonical models: rigid bodies, geometrically exact beams, and solid-degenerate shells. Beams and shells are discretised using the FE method. The subsequent section describes the fundamental equations and main ideas of the framework and briefly shows the spatial and temporal discretisations. For more details, we refer the reader to the aforementioned literature.

## 2.1 Continuous governing equation

Based on the primal-dual variational principle, for a material body $\mathcal{B}_0 \subseteq \mathbb{R}^3$, the continuous governing equation of the constrained system is determined by

$$\begin{aligned} \delta S = \int_{\mathcal{B}_0} \big( &\langle \delta \mathbf{v}, \mathbf{l}(\mathbf{v},t) - \mathbf{l}(\dot{\mathbf{x}},t) \rangle + \langle \delta \boldsymbol{\lambda}, \mathbf{h}(\mathbf{x},t) \rangle \\ &+ \langle \delta \mathbf{x}, \dot{\mathbf{l}}(\mathbf{v},t) + \mathbf{f}^{\mathrm{int}}(\mathbf{x},t) - \mathbf{f}^{\mathrm{ext}}(t) + \mathbf{H}(\mathbf{x},t)^{\mathrm{T}} \boldsymbol{\lambda}(t) \rangle \big) dV = 0. \end{aligned} \tag{1}$$

Herein $\langle \cdot, \cdot \rangle$ denotes a scalar product and $\delta(\cdot)$ the admissible variation of a given quantity. The positions and velocities of a material point are denoted by $\mathbf{x}(\theta_i, t) = \boldsymbol{\Theta} \cdot \mathbf{q}$ and $\mathbf{v}(\theta_i, t) = \boldsymbol{\Theta} \cdot \mathbf{s}$, respectively. These specifically depend on the canonical model. $\theta_i$, with $i = 1, 2, 3$, specifying the coordinates of a material point in the director coordinate system of a reference point of a canonical model. $\boldsymbol{\Theta}$ is the vector of the director coordinates $\theta_i$. $\mathbf{q}$ and $\mathbf{s}$ are vectors of the generalised coordinates and velocities, considering the kinematics. As a mixed formulation is used, the equivalence of the displacement-based and velocity-based momentum densities is incorporated into equation 1 by using $\mathbf{l}(\dot{\mathbf{x}}, t)$ and $\mathbf{l}(\mathbf{v}, t)$, respectively. Inertia terms are taken into account by the time derivative of the velocity-based momentum density $\dot{\mathbf{l}}(\mathbf{v}, t)$. $\mathbf{f}^{\mathrm{int}}(\mathbf{x}, t)$ and $\mathbf{f}^{\mathrm{ext}}(t)$ are the internal and external force densities, respectively. $\mathbf{h}(\mathbf{x}, t)$ represents a set of kinematic restrictions and $\boldsymbol{\lambda}(t)$ a vector of Lagrange-multipliers. $\mathbf{H}(\mathbf{x}, t)$ is the

Jacobian of the holonomic constraints.
A three-director formulation is chosen, with the directors denoted by $\mathbf{d}_i$ and $i = 1, 2, 3$. The additive update of the rotation in the total Lagrangian description ensures the path-independence. With the outer product $\cdot \otimes \cdot$ and the standard euclidean basis $\mathbf{e}_i$, the rotational tensor $\mathbf{R}$ is represented by

$$\mathbf{R} = \mathbf{d}_1 \otimes \mathbf{e}_1 + \mathbf{d}_2 \otimes \mathbf{e}_2 + \mathbf{d}_3 \otimes \mathbf{e}_3. \tag{2}$$

As we will refer to the kinetic and elastic strain energy later, they are subsequently introduced. The mass density per unit volume $\rho$ and the constant symmetric mass matrix $\mathbf{M}$ lead to the kinetic energy $T$:

$$T = \frac{1}{2} \int_{\mathcal{B}_0} \rho \langle \mathbf{v}(\theta_i, t), \mathbf{v}(\theta_i, t) \rangle dV \tag{3}$$

The elastic strain energy $W$ of the mechanical system is given by:

$$W = \int_{\mathcal{B}0} \langle \delta\mathbf{x}, \mathbf{f}^{\text{int}}(\mathbf{x}, t) \rangle dV = \int_{\mathcal{B}_0} \langle \delta\mathbf{E}(\mathbf{x}), \mathbf{S} \rangle dV. \tag{4}$$

Herein $\mathbf{E}$ denotes the Green-Lagrange strain tensor and $\mathbf{S}$ the corresponding work-conjugated stress tensor, here the second Piola-Kirchhoff stress tensor. The Green-Lagrange strain tensor is defined as (see [26]):

$$\mathbf{E} = \frac{1}{2}(\mathbf{F}(t)^{\mathrm{T}}\mathbf{F}(t) - \mathbf{F}(0)^{\mathrm{T}}\mathbf{F}(0)), \tag{5}$$

with $\mathbf{F}$ being the tangent map (also referred to as deformation gradient). Of course, no elastic energy is stored in rigid bodies. For a more detailed discussion of the strain tensor in terms of the geometrically exact beam analysis we refer to [27] and [28].

## 2.2 Discretisation of the governing equation in space and time

To spatially and temporally discretise equation 1, we first have to substitute the coordinates and velocities $\mathbf{x}$ and $\mathbf{v}$ by a set of generalised coordinates and velocities $\mathbf{q}$ and $\mathbf{s}$. Here, the kinematics of the respective canonical model are taken into account, see [28].
Equation 1 is spatially discretised using the FE method. We use two-node elements and linear Lagrange-type shape functions. The solid-degenerate shell elements use bilinear shape functions and two-point Gaussian quadrature in thickness direction. In order to maintain the orthogonality as well as the initial length $||\mathbf{d}_i(0)|| = 1$ of the director triad in each node a set of internal constraints is applied, see [14].
The framework employs an implicit time integration scheme. It is based on the midpoint rule and the *average-vector-field* method and preserves the linear and angular momentum as well as the total energy of the system in order to ensure physical correctness and robustness. For a detailed description of the temporal discretisation, see [14], where this method is discussed extensively.

Following the mid-point rule, the configuration and the generalised velocities are approximated in between two time steps $t_{n+\frac{1}{2}} = \frac{1}{2}(t_{n+1} - t_n)$, with the time steps $n$ and $n+1$ and the time step size $\Delta t = t_{n+1} - t_n$ as

$$\mathbf{q}_{t_{n+\frac{1}{2}}} \approx \frac{\mathbf{q}_{t_n} + \mathbf{q}_{t_{n+1}}}{2}, \quad \mathbf{s}_{t_{n+\frac{1}{2}}} \approx \frac{\mathbf{s}_{t_n} + \mathbf{s}_{t_{n+1}}}{2}. \tag{6}$$

The evaluation of the governing equation, using equation 6, leads to its spatially and temporally discrete form, denoted in equation 7. The superscript $(\cdot)^d$ indicates a spatially discrete quantity.

$$\begin{aligned} \delta S^d_{t_{n+1}} =& \big( \langle \delta \mathbf{s}^d_{t_{n+1}}, \mathbf{l}^d(\mathbf{s}^d_{t_{n+1}}, \mathbf{s}^d_{t_n}) - \mathbf{l}^d(\dot{\mathbf{q}}^d_{t_{n+1}}, \dot{\mathbf{q}}^d_{t_n}) \rangle + \langle \delta \boldsymbol{\lambda}^d_{t_{n+1}}, \mathbf{h}^d(\mathbf{q}_{t_{n+1}}, \mathbf{q}^d_{t_n}) \rangle \\ &+ \langle \delta \mathbf{q}^d_{t_{n+\frac{1}{2}}}, \dot{\mathbf{l}}^d(\mathbf{s}^d_{t_{n+1}}, \mathbf{s}^d_{t_n}) + \mathbf{f}^{\mathrm{int,d}}(\mathbf{q}^d_{t_{n+1}}, \mathbf{q}^d_{t_n}) - \mathbf{f}^{\mathrm{ext,d}}(\mathbf{q}^d_{t_{n+1}}, \mathbf{q}^d_{t_n}) \\ &+ \mathbf{H}^{d^{\mathrm{T}}}(\mathbf{q}^d_{t_{n+1}}, \mathbf{q}^d_{t_n}) \boldsymbol{\lambda}^d_{t_{n+\frac{1}{2}}} \rangle \big) = 0, \end{aligned} \tag{7}$$

see also [14]. In the discretised form we consider non-conservative forces in the discrete vector of internal forces $\mathbf{f}^{\mathrm{int},d}(\mathbf{q}^d_{t_{n+1}}, \mathbf{q}^d_{t_n})$ and in the velocity-based momentum $\mathbf{l}^d(\mathbf{s}^d_{t_{n+1}}, \mathbf{s}^d_{t_n})$ as strain/stress and velocity dependent energy dissipation can be added to the geometrically exact beams and the solid-degenerate shells [19]. Equation 7, in its discrete form can also contain non-conservative forces in $\mathbf{f}^{\mathrm{ext},d}(\mathbf{q}^d_{t_{n+1}}, \mathbf{q}^d_{t_n})$. Although it is theoretically possible to consider higher order dissipation functions, we restrict ourselves to first-order dissipation functions. As we handle from now on exclusively spatially and temporally discrete quantities, the superscript $(\cdot)^d$ is omitted again. Equation 7 has to be true for arbitrary variations which leads to the nonlinear spatially and temporally discrete governing equation of the mechanical framework

$$\mathbf{g}(\mathbf{q}_{t_{n+1}}, \mathbf{s}_{t_{n+1}}, \boldsymbol{\lambda}_{t_{n+1}}) = \begin{bmatrix} \mathbf{f}^{\mathrm{int}}(\mathbf{q}) - \mathbf{f}^{\mathrm{ext}}(\mathbf{q}) + \dot{\mathbf{l}}(\mathbf{s}) + \mathbf{H}^{\mathrm{T}}(\mathbf{q}) \boldsymbol{\lambda} \\ \mathbf{l}(\mathbf{s}) - \mathbf{l}(\mathbf{q}) \\ \mathbf{h}(\mathbf{q}) \end{bmatrix}_{t_{n+1}} = \mathbf{0}. \tag{8}$$

## 2.3 Solving algorithm

The unknown state variables in the nonlinear governing equation 8 are the generalised coordinates $\mathbf{q}_{t_{n+1}}$, the generalised velocities $\mathbf{s}_{t_{n+1}}$ and the Lagrange-multipliers $\boldsymbol{\lambda}_{t_{n+1}}$, each at the next time step $t_{n+1}$. This nonlinear governing equation is solved iteratively using Newton's method. We solve for the unknown relative increments $\Delta\mathbf{q}$, $\Delta\mathbf{s}$ and $\Delta\boldsymbol{\lambda}$ at the iteration step $k$

$$\begin{aligned} \mathbf{g}(\mathbf{q}_{t_{n+1}}, \mathbf{s}_{t_{n+1}}, \boldsymbol{\lambda}_{t_{n+1}})^{k+1} =& \mathbf{g}(\mathbf{q}_{t_{n+1}}, \mathbf{s}_{t_{n+1}}, \boldsymbol{\lambda}_{t_{n+1}})^k \\ &+ \Delta_G \mathbf{g}(\mathbf{q}_{t_{n+1}}, \mathbf{s}_{t_{n+1}}, \boldsymbol{\lambda}_{t_{n+1}})^k = \mathbf{0}. \end{aligned} \tag{9}$$

Here $\Delta_G(\cdot) = \frac{\partial(\cdot)}{\partial \mathbf{q}} \Delta_k \mathbf{q} + \frac{\partial(\cdot)}{\partial \mathbf{s}} \Delta_k \mathbf{s} + \frac{\partial(\cdot)}{\partial \boldsymbol{\lambda}} \Delta_k \boldsymbol{\lambda}$ is the Gâteaux-derivative. The term $\Delta_G \mathbf{g}(\mathbf{q}_{t_{n+1}}, \mathbf{s}_{t_{n+1}}, \boldsymbol{\lambda}_{t_{n+1}})^k$ is consequently the incremental form of the nonlinear governing equation $\mathbf{g}(\mathbf{q}_{t_{n+1}}, \mathbf{s}_{t_{n+1}}, \boldsymbol{\lambda}_{t_{n+1}})^k$ at the time instant $t_{n+1}$ and the iteration step

$k$, following Newton's method. Substituting the governing equation 8 into the Newton's method 9, we obtain the following matrix formulation

$$\begin{aligned}\begin{bmatrix}\mathbf{0}\\ \mathbf{0}\\ \mathbf{0}\end{bmatrix} &= \begin{bmatrix}\mathbf{f}^{\text{int}}(\mathbf{q}) - \mathbf{f}^{\text{ext}}(\mathbf{q}) + \dot{\mathbf{l}}(\mathbf{s}) + \mathbf{H}^{T}(\mathbf{q})\boldsymbol{\lambda}\\ \mathbf{l}(\mathbf{s}) - \mathbf{l}(\mathbf{q})\\ \mathbf{h}(\mathbf{q})\end{bmatrix}^{k}_{t_{n+1}}\\ &+ \begin{bmatrix}\mathbf{K}_{\text{int}}(\mathbf{q}) - \mathbf{K}_{\text{ext}}(\mathbf{q}) + \mathbf{K}_{\lambda\lambda}(\mathbf{q}) & \mathbf{K}_{qs} & \mathbf{H}^{\text{T}}(\mathbf{q})\\ \mathbf{K}_{sq} & \mathbf{K}_{ss}(\mathbf{s}) & \mathbf{0}\\ \mathbf{H}(\mathbf{q}) & \mathbf{0} & \mathbf{0}\end{bmatrix}^{k}_{t_{n+1}} \cdot \begin{bmatrix}\Delta_k\mathbf{q}\\ \Delta_k\mathbf{s}\\ \Delta_k\boldsymbol{\lambda}\end{bmatrix}.\end{aligned} \tag{10}$$

The iteration matrix is composed as follows:

$$\begin{aligned}&\mathbf{K}_{\text{int}}(\mathbf{q}) = \frac{\partial \mathbf{f}^{\text{int}}(\mathbf{q})}{\partial \mathbf{q}}, && \mathbf{K}_{\text{ext}}(\mathbf{q}) = \frac{\partial \mathbf{f}^{\text{ext}}(\mathbf{q})}{\partial \mathbf{q}}, && \mathbf{K}_{qs} = \frac{\partial \dot{\mathbf{l}}(\mathbf{s})}{\partial \mathbf{s}},\\ &\mathbf{K}_{\lambda\lambda}(\mathbf{q}) = \frac{\partial \mathbf{H}^{\text{T}}(\mathbf{q})}{\partial \mathbf{q}}, && \mathbf{H}^{\text{T}}(\mathbf{q}) = \frac{\partial \mathbf{H}^{\text{T}}(\mathbf{q})\boldsymbol{\lambda}}{\partial \boldsymbol{\lambda}}, && \mathbf{K}_{sq} = \frac{\partial \mathbf{l}(\mathbf{q})}{\partial \mathbf{q}},\\ &\mathbf{K}_{ss}(\mathbf{s}) = \frac{\partial \mathbf{l}(\mathbf{s})}{\partial \mathbf{s}}, && \mathbf{H}(\mathbf{q}) = \frac{\partial \mathbf{h}(\mathbf{q})}{\partial \mathbf{q}}.\end{aligned} \tag{11}$$

$\Delta_k(\cdot) = (\cdot)^{k+1}_{t_{n+1}} - (\cdot)^{k}_{t_{n+1}}$ denotes the change of a respective quantity between two iteration steps . If terms in the governing equation are added, this must of course be taken into account by adjusting its derivatives in the iteration matrix to preserve the robust quadratic convergence rate of the solving algorithm [29].

# 3 Derivation of the geometrically exact coupling element

In this section we derive the element equations according to equations 8 and 9, i.e., all element forces and moments of the general node-to-node coupling element, including stiffness, mass and damping. The same element can also be utilised to couple a node with the surrounding environment. As stated previously, the mechanical equations for the coupling element provide a consistent extension of the mechanical framework described in [13–20] and briefly introduced in section 2. It allows the geometrically exact consideration of flexible joints, such as the adhesive bonding of two mechanical components with large displacements and rotations [3] or bushing elements in automotive suspensions [6]. Objectivity and path-independence are maintained. Due to the geometrically exact formulation, stability analyses can be performed taking into account the flexible connection. Due to the considered inertia terms, the coupling element can be taken into account in modal analyses. In this work we focus on the coupling of nodes with three-directors. Consequently, rigid bodies and geometrically exact beams can be coupled. An extension for nodes with one director, e.g., solid-degenerate shells can be easily performed.
Figure 1 illustrates schematically the coupling element applied between two nodes $A$

and $B$. The Euclidean standard basis $\mathbf{e}_i$ and the position vectors $\overline{\mathbf{x}}^A$, $\overline{\mathbf{x}}^B$ and the director triads $\mathbf{d}_i^A$ and $\mathbf{d}_i^B$ are shown. Due to the director-based formulation, generalised

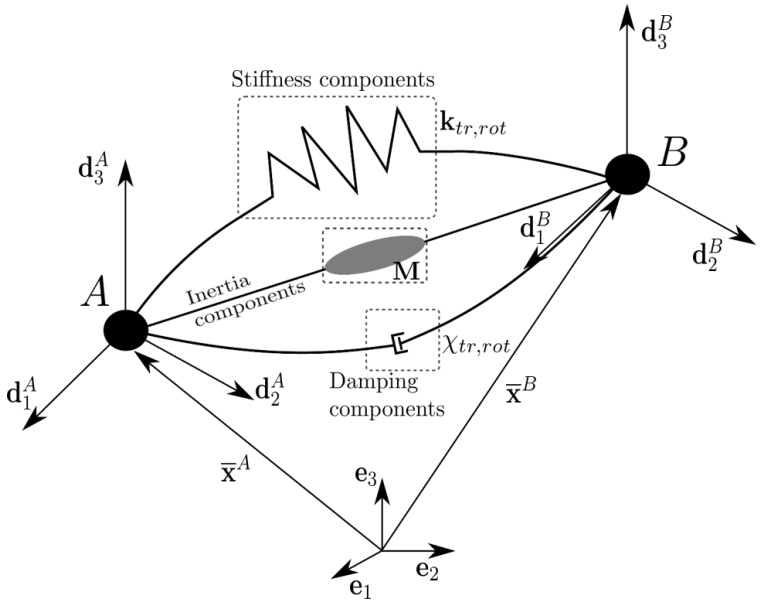


**Fig. 1** Schematic representation of the coupling element connecting two nodes

coordinates and generalised velocities are used. The generalised coordinates consist of a vector to a reference point $\overline{\mathbf{x}}$ belonging to the respective canonical model and the orthonormal directors $\mathbf{d}_i$ at that reference position

$$\mathbf{q}(t) = [\overline{\mathbf{x}}(t), \mathbf{d}_1(t), \mathbf{d}_2(t), \mathbf{d}_3(t)]^{\mathrm{T}} \in \mathbb{R}^{12\times 1}. \tag{12}$$

The velocity of the reference point is given by $\overline{\mathbf{v}}$. The velocity of the director triad is denoted $\mathbf{w}_i$ leading to the vector of generalised velocities.

$$\mathbf{s}(t) = [\overline{\mathbf{v}}(t), \mathbf{w}_1(t), \mathbf{w}_2(t), \mathbf{w}_3(t)]^{\mathrm{T}} \in \mathbb{R}^{12\times 1}. \tag{13}$$

## 3.1 Derivation and linearisation of the internal forces

In this contribution, we introduce a coupling element with a formulation that is consistent with that of the geometrically exact beam. This ensures objectivity and allows geometrically exact kinematics to be mapped.
We propose an objective strain measure inspired by the Green-Lagrange strain tensor. It is important to note that other deformation measures can also be used, provided that they satisfy the necessary properties. As discussed in [27, 28, 30, 31], the Green-Lagrange strain tensor can be decomposed into two work-conjugate strain vectors of

axial strains and curvatures. This is also applied to the deformation measure of the coupling element, leading to

$$\Gamma_i = \langle \mathbf{A}(\mathbf{d}_i(t)), \mathbf{D}(\mathbf{x}(t)) \rangle - \langle \mathbf{A}(\mathbf{d}_i(t_0)), \mathbf{D}(\mathbf{x}(t_0)) \rangle, \tag{14}$$

$$\Omega_i = \frac{1}{2} \varepsilon_{ijk} [\langle \mathbf{A}(\mathbf{d}_k(t)), \mathbf{D}(\mathbf{d}_j(t)) \rangle - \langle \mathbf{A}(\mathbf{d}_k(t_0)), \mathbf{D}(\mathbf{d}_j(t_0)) \rangle]. \tag{15}$$

Here $\Gamma_i$ denote the axial strains, $\Omega_i$ denote the curvatures and $t_0 = t(0)$. $\varepsilon_{ijk}$ is the permutation symbol. $\mathbf{A}(\cdot)$ and $\mathbf{D}(\cdot)$ symbolize an average and a discrete differential operator, respectively, defined as

$$\mathbf{A}(\mathbf{d}_i) = \frac{\mathbf{d}_i^A + \mathbf{d}_i^B}{2}, \quad \mathbf{D}(\overline{\mathbf{x}}) = \frac{\overline{\mathbf{x}}^B - \overline{\mathbf{x}}^A}{\eta}. \tag{16}$$

The superscripts $(\cdot)^A$ and $(\cdot)^B$ indicate the nodes, between which the coupling element is implemented. $\eta$ is a parameter with the dimension of a length. If one substitutes the relations denoted in equation 16 into equations 14 and 15, we obtain

$$\mathbf{\Gamma} = \frac{1}{2\eta} \begin{bmatrix} \langle \overline{\mathbf{x}}^{B,t} - \overline{\mathbf{x}}^{A,t}, \mathbf{d}_1^{A,t} + \mathbf{d}_1^{B,t} \rangle - \langle \overline{\mathbf{x}}^{B,0} - \overline{\mathbf{x}}^{A,0}, \mathbf{d}_1^{A,0} + \mathbf{d}_1^{B,0} \rangle \\ \langle \overline{\mathbf{x}}^{B,t} - \overline{\mathbf{x}}^{A,t}, \mathbf{d}_2^{A,t} + \mathbf{d}_2^{B,t} \rangle - \langle \overline{\mathbf{x}}^{B,0} - \overline{\mathbf{x}}^{A,0}, \mathbf{d}_2^{A,0} + \mathbf{d}_2^{B,0} \rangle \\ \langle \overline{\mathbf{x}}^{B,t} - \overline{\mathbf{x}}^{A,t}, \mathbf{d}_3^{A,t} + \mathbf{d}_3^{B,t} \rangle - \langle \overline{\mathbf{x}}^{B,0} - \overline{\mathbf{x}}^{A,0}, \mathbf{d}_3^{A,0} + \mathbf{d}_3^{B,0} \rangle \end{bmatrix}, \tag{17}$$

$$\mathbf{\Omega} = \frac{1}{2\eta} \begin{bmatrix} \langle \mathbf{d}_2^{A,t}, \mathbf{d}_3^{B,t} \rangle - \langle \mathbf{d}_3^{A,t}, \mathbf{d}_2^{B,t} \rangle - \langle \mathbf{d}_2^{A,0}, \mathbf{d}_3^{B,0} \rangle + \langle \mathbf{d}_3^{A,0}, \mathbf{d}_2^{B,0} \rangle \\ \langle \mathbf{d}_3^{A,t}, \mathbf{d}_1^{B,t} \rangle - \langle \mathbf{d}_1^{A,t}, \mathbf{d}_3^{B,t} \rangle - \langle \mathbf{d}_3^{A,0}, \mathbf{d}_1^{B,0} \rangle + \langle \mathbf{d}_1^{A,0}, \mathbf{d}_3^{B,0} \rangle \\ \langle \mathbf{d}_1^{A,t}, \mathbf{d}_2^{B,t} \rangle - \langle \mathbf{d}_2^{A,t}, \mathbf{d}_1^{B,t} \rangle - \langle \mathbf{d}_1^{A,0}, \mathbf{d}_2^{B,0} \rangle + \langle \mathbf{d}_2^{A,0}, \mathbf{d}_1^{B,0} \rangle \end{bmatrix}. \tag{18}$$

The subscripts $(\cdot)^t$ and $(\cdot)^0$ indicate the time instant $t$ or the initial time $t = t_0$, respectively. Summarized in a deformation vector $\mathbf{U}$, defined as

$$\mathbf{U} = \begin{bmatrix} \mathbf{\Gamma} \\ \mathbf{\Omega} \end{bmatrix} \in \mathbb{R}^{6 \times 1}. \tag{19}$$

As these are work-conjugate strain components the axial and transverse shear forces $\mathbf{F} \in \mathbb{R}^{3 \times 1}$ as well as the torsional and bending moments $\mathbf{M} \in \mathbb{R}^{3 \times 1}$ can be obtained by deriving the elastic potential $W(\mathbf{\Gamma}, \mathbf{\Omega})$ with respect to the strain components

$$\mathbf{F} = \frac{\partial W_{int}}{\partial \mathbf{\Gamma}} \quad \text{and} \quad \mathbf{M} = \frac{\partial W_{int}}{\partial \mathbf{\Omega}}, \tag{20}$$

providing such exists. Note that $\mathbf{F}$ refers here and following to the force components and not to the tangent map.

The coupling element allows to employ a fully populated elasticity matrix $\mathbf{C}$

$$\mathbf{C} = \left[\begin{array}{ccc:ccc} c_{11} & c_{12} & c_{13} & c_{14} & c_{15} & c_{16} \\ c_{21} & c_{22} & c_{23} & c_{24} & c_{25} & c_{26} \\ c_{31} & c_{32} & c_{33} & c_{34} & c_{35} & c_{36} \\ \hdashline c_{41} & c_{42} & c_{43} & c_{44} & c_{45} & c_{46} \\ c_{51} & c_{52} & c_{53} & c_{54} & c_{55} & c_{56} \\ c_{61} & c_{62} & c_{63} & c_{64} & c_{65} & c_{66} \end{array}\right] = \left[\begin{array}{c:c} \mathbf{C}_{\mathbf{\Gamma\Gamma}} & \mathbf{C}_{\mathbf{\Gamma\Omega}} \\ \hdashline \mathbf{C}_{\mathbf{\Gamma\Omega}}^{\mathrm{T}} & \mathbf{C}_{\mathbf{\Omega\Omega}} \end{array}\right]. \tag{21}$$

The subscripts $\mathbf{\Gamma}$ and $\mathbf{\Omega}$ indicate the axial and transverse shear forces and the torsional and bending moments affected by the entries, respectively. $\mathbf{C}_{\mathbf{\Gamma\Gamma}}$ and $\mathbf{C}_{\mathbf{\Omega\Omega}}$ are symmetric about their diagonal, $\mathbf{C}_{\mathbf{\Gamma\Omega}} = \mathbf{C}_{\mathbf{\Omega\Gamma}}^{\mathrm{T}}$ are skew-symmetric matrices.
We subsequently derive the internal forces and moments caused by the elasticity of the coupling element. Therefore, we consider the variation of the strain energy, according to the principle of virtual work, as

$$\delta W_{int} = \left\langle \delta\mathbf{\Gamma}^{\mathrm{T}}, \mathbf{F} \right\rangle + \left\langle \delta\mathbf{\Omega}^{\mathrm{T}}, \mathbf{M} \right\rangle \tag{22}$$

with the admissible variation $\delta(\cdot)$. This leads to

$$\delta W_{int} = \delta\mathbf{q}^{\mathrm{T}} \left[ \left(\frac{\partial\mathbf{\Gamma}}{\partial\mathbf{q}}\right)^{\mathrm{T}} \left(\frac{\partial\mathbf{\Omega}}{\partial\mathbf{q}}\right)^{\mathrm{T}} \right] \left[\begin{array}{c} \mathbf{F} \\ \mathbf{M} \end{array}\right] = \delta\mathbf{q}^{\mathrm{T}}\mathbf{B}^{\mathrm{T}}\mathbf{N}. \tag{23}$$

$\mathbf{B}^{\mathrm{T}} \in \mathbb{R}^{24\times 6}$ is a differential operator, $\mathbf{N} \in \mathbb{R}^{6\times 1}$ is the combined vector of forces and moments

$$\mathbf{N} = \mathbf{C}\mathbf{U} = \mathbf{C}(\mathbf{B}^{\mathrm{T}}\mathbf{q}). \tag{24}$$

Carrying out the derivations introduced by the variation in equation 23, for the differential operator $\mathbf{B}^{\mathrm{T}}$ follows

$$\mathbf{B}^{\mathrm{T}} = \frac{1}{2\eta} \begin{bmatrix} -(\mathbf{d}_1^A + \mathbf{d}_1^B) & -(\mathbf{d}_2^A + \mathbf{d}_2^B) & -(\mathbf{d}_3^A + \mathbf{d}_3^B) & \mathbf{0} & \mathbf{0} & \mathbf{0} \\ (\mathbf{x}^B - \mathbf{x}^A) & \mathbf{0} & \mathbf{0} & \mathbf{0} & -\mathbf{d}_3^B & \mathbf{d}_2^B \\ \mathbf{0} & (\mathbf{x}^B - \mathbf{x}^A) & \mathbf{0} & \mathbf{d}_3^B & \mathbf{0} & -\mathbf{d}_1^B \\ \mathbf{0} & \mathbf{0} & (\mathbf{x}^B - \mathbf{x}^A) & -\mathbf{d}_2^B & \mathbf{d}_1^B & \mathbf{0} \\ (\mathbf{d}_1^A + \mathbf{d}_1^B) & (\mathbf{d}_2^A + \mathbf{d}_2^B) & (\mathbf{d}_3^A + \mathbf{d}_3^B) & \mathbf{0} & \mathbf{0} & \mathbf{0} \\ (\mathbf{x}^B - \mathbf{x}^A) & \mathbf{0} & \mathbf{0} & \mathbf{0} & \mathbf{d}_3^A & -\mathbf{d}_2^A \\ \mathbf{0} & (\mathbf{x}^B - \mathbf{x}^A) & \mathbf{0} & -\mathbf{d}_3^A & \mathbf{0} & \mathbf{d}_1^A \\ \mathbf{0} & \mathbf{0} & (\mathbf{x}^B - \mathbf{x}^A) & \mathbf{d}_2^A & -\mathbf{d}_1^A & \mathbf{0} \end{bmatrix}. \tag{25}$$

According to the time integration scheme presented in section 2, equation 25 is evaluated at the temporal midpoint. The discrete elastic force vector $\mathbf{f}^{\mathrm{int}} \in \mathbb{R}^{24\times 1}$ is given as

$$\mathbf{f}^{\mathrm{int}} = \mathbf{B}^{\mathrm{T}}\mathbf{N}. \tag{26}$$

The term of discrete internal forces of the coupling element is added to the discrete internal forces of the overall system in equation 8. To apply Newton's method in order to solve the nonlinear governing equation, we have to linearise the added discrete elastic forces, according to equation 9. Respecting the product rule, we obtain

$$\Delta_G \delta W = \Delta_G(\delta \mathbf{q}^{\mathrm{T}} \mathbf{B}^{\mathrm{T}} \mathbf{N}) = \delta \mathbf{q}^{\mathrm{T}} \Delta_G(\mathbf{f}^{\mathrm{int}}). \tag{27}$$

As $\mathbf{B}^{\mathrm{T}}(\mathbf{q})$ and $\mathbf{N}(\mathbf{q})$ depend on the generalized coordinates $\mathbf{q}$, again the product rule is applied

$$\Delta_G(\mathbf{f}^{\mathrm{int}}) = \Delta_G(\mathbf{B}^{\mathrm{T}}\mathbf{N}) = \left( \underbrace{\frac{\partial}{\partial \mathbf{q}}(\mathbf{B}^{\mathrm{T}}\mathbf{C}\mathbf{B}^{\mathrm{T}}\mathbf{q})}_{\mathrm{I}} \Bigg|_{\mathbf{q}=\mathrm{const.}} + \underbrace{\frac{\partial}{\partial \mathbf{q}}(\mathbf{B}^{\mathrm{T}}\mathbf{N})}_{\mathrm{II}} \Bigg|_{\mathbf{N}=\mathrm{const.}} \right) \Delta_k \mathbf{q}. \tag{28}$$

Following the two terms are linearised separately. The linearisation of the first term yields

$$\begin{aligned} \Delta_G \mathbf{N} &= \frac{\partial}{\partial \mathbf{q}} \Big( \mathbf{C}\mathbf{B}^{\mathrm{T}}\mathbf{q} \Big) \Delta_k \mathbf{q} = \left( \frac{\partial}{\partial \mathbf{q}} \Big( \mathbf{C}\mathbf{B}^{\mathrm{T}}\mathbf{q} \Big) \Big|_{\mathbf{q}=\mathbf{const.}} + \mathbf{C}\mathbf{B}^{\mathrm{T}} \right) \Delta_k \mathbf{q} \\ &= \Big( \mathbf{C}\mathbf{B}^{\mathrm{T}} \Big) \Delta_k \mathbf{q}, \end{aligned} \tag{29}$$

with the given elasticity matrix $\mathbf{C} \in \mathbb{R}^{6\times 6}$ in Voigt notation of the coupling element. The linarisation of the second term of equation 28 leads to

$$\frac{\partial}{\partial \mathbf{q}}(\mathbf{B}^{\mathrm{T}}\mathbf{N}) \Big|_{\mathbf{N}=\mathrm{const.}} \Delta \mathbf{q} = \mathbf{K}_{\mathrm{stress}} \Delta_k \mathbf{q}, \tag{30}$$

with

$$\mathbf{K}_{\mathrm{stress}} = \frac{1}{2\eta} \begin{bmatrix} \mathbf{0} & -F_1\mathbf{I} & -F_2\mathbf{I} & -F_3\mathbf{I} & \mathbf{0} & -F_1\mathbf{I} & -F_2\mathbf{I} & -F_3\mathbf{I} \\ -F_1\mathbf{I} & \mathbf{0} & \mathbf{0} & \mathbf{0} & F_1\mathbf{I} & \mathbf{0} & M_3\mathbf{I} & -M_2\mathbf{I} \\ -F_2\mathbf{I} & \mathbf{0} & \mathbf{0} & \mathbf{0} & F_2\mathbf{I} & -M_3\mathbf{I} & \mathbf{0} & M_1\mathbf{I} \\ -F_3\mathbf{I} & \mathbf{0} & \mathbf{0} & \mathbf{0} & F_3\mathbf{I} & M_2\mathbf{I} & -M_1\mathbf{I} & \mathbf{0} \\ \mathbf{0} & F_1\mathbf{I} & F_2\mathbf{I} & F_3\mathbf{I} & \mathbf{0} & F_1\mathbf{I} & F_2\mathbf{I} & F_3\mathbf{I} \\ -F_1\mathbf{I} & \mathbf{0} & -M_3\mathbf{I} & M_2\mathbf{I} & F_1\mathbf{I} & \mathbf{0} & \mathbf{0} & \mathbf{0} \\ -F_2\mathbf{I} & M_3\mathbf{I} & \mathbf{0} & -M_1\mathbf{I} & F_2\mathbf{I} & \mathbf{0} & \mathbf{0} & \mathbf{0} \\ -F_3\mathbf{I} & -M_2\mathbf{I} & M_1\mathbf{I} & \mathbf{0} & F_3\mathbf{I} & \mathbf{0} & \mathbf{0} & \mathbf{0} \end{bmatrix}. \tag{31}$$

If one substitutes the results of the derivation back into equation 27 we obtain

$$\Delta_G \delta W = \mathbf{K}_{\mathrm{int}} = \delta \mathbf{q} \big( \underbrace{\mathbf{B}^{\mathrm{T}}\mathbf{C}\mathbf{B}}_{\mathbf{K}_m} + \mathbf{K}_{\mathrm{stress}} \big) \Delta_k \mathbf{q}$$

$$= \delta\mathbf{q}\big(\mathbf{K}_m + \mathbf{K}_{\text{stress}}\big)\Delta_k\mathbf{q}. \tag{32}$$

Here $\mathbf{K}_{\text{stress}}$ represents the stress dependent stiffness contribution and $\mathbf{K}_m$ the material stiffness contribution.

## 3.2 Derivation of the inertia forces

To introduce mass properties into the coupling element, we have chosen a formulation equivalent to an arbitrarily shaped continuum modelled as a lumped element. This formulation is not equivalent to adding masses to the coupled nodes or elements. There are two reasons for this. Firstly, the location of the added masses would be different from the location of the coupling element mass and therefore the dynamic behaviour would be affected. Secondly, the mass distribution in the coupling is not taken into account. The mass matrix of an arbitrarily shaped continuum can be derived as follows. The kinetic energy is denoted as

$$T_{\text{ac}} = \frac{1}{2}\int_{\theta^3}\int_{\theta^2}\int_{\theta^1}\langle\rho\mathbf{v}_{\text{ac}}^{\text{T}}, \mathbf{v}_{\text{ac}}\rangle \text{d}\theta^1\text{d}\theta^2\text{d}\theta^3. \tag{33}$$

We write the velocity in matrix notation

$$\mathbf{v}_{\text{ac}} = \begin{bmatrix} 1 & \theta^1 & \theta^2 & \theta^3 \end{bmatrix} \begin{bmatrix} \overline{\mathbf{v}} \\ \mathbf{w}_1 \\ \mathbf{w}_2 \\ \mathbf{w}_3 \end{bmatrix} = \boldsymbol{\Theta}\mathbf{s}_{\text{ac}} \tag{34}$$

and obtain the constant mass matrix of the continuous element

$$\mathbf{M}_{\text{ac}} = \int_{\theta^3}\int_{\theta^2}\int_{\theta^1}\boldsymbol{\Theta}^{\text{T}}\rho\boldsymbol{\Theta}\text{d}\theta^1\text{d}\theta^2\text{d}\theta^3 = \int_{\mathcal{B}_0}\boldsymbol{\Theta}^{\text{T}}\rho\boldsymbol{\Theta}dV. \tag{35}$$

This mass is assumed to be located between the connected nodes $A$ and $B$, as shown schematically in figure 1. It remains at the centre of the concerned nodes at all times and is not weighted along the length of the element.
To derive the inertia forces acting on the connected nodes, we need the mass matrix of the coupling element with equivalent properties as just shown for the arbitrarily shaped continuum. It can be obtained by writing down the kinetic energy of the coupling element. All quantities without subscripts refer to the coupling element.

$$T = \frac{1}{2}\Big\langle\mathbf{s}^{AB}, \mathbf{M}_{\text{ac}}\mathbf{s}^{AB}\Big\rangle. \tag{36}$$

$\mathbf{s}^{AB}$ denotes the velocity of the midpoint between the nodes. Consequently, it is determined as follows:

$$\mathbf{s}^{AB} = \frac{\mathbf{s}^A + \mathbf{s}^B}{2}, \tag{37}$$

with the generalised velocities of $\mathbf{s}^A$ and $\mathbf{s}^B$ of the respective nodes. Substituting the velocity $\mathbf{s}^{AB}$ in equation 36, allows to determine the mass matrix $\mathbf{M}_{\text{ce}}$ of the coupling element.

$$\begin{aligned} T &= \frac{1}{2}\Big\langle \Big(\frac{\mathbf{s}^A + \mathbf{s}^B}{2}\Big), \mathbf{M}_{\text{ac}} \Big(\frac{\mathbf{s}^A + \mathbf{s}^B}{2}\Big)\Big\rangle \\ &= \frac{1}{2}\Big\langle \begin{bmatrix} \mathbf{s}^{A^{\mathrm{T}}} & \mathbf{s}^{B^{\mathrm{T}}} \end{bmatrix}, \mathbf{M}_{\text{ce}} \begin{bmatrix} \mathbf{s}^A \\ \mathbf{s}^B \end{bmatrix}\Big\rangle, \end{aligned} \tag{38}$$

with

$$\mathbf{M}_{\text{ce}} = \frac{1}{4}\begin{bmatrix} \mathbf{M}_{\text{ac}} & \mathbf{M}_{\text{ac}} \\ \mathbf{M}_{\text{ac}} & \mathbf{M}_{\text{ac}} \end{bmatrix}. \tag{39}$$

The acceleration of the nodes in equation 7 are determined using the discrete time derivative of the nodes' generalised velocities

$$\dot{\mathbf{s}}^A_{t_{n+\frac{1}{2}}} \approx \frac{\mathbf{s}^A_{t_{n+1}} - \mathbf{s}^A_{t_n}}{\Delta t}, \quad \dot{\mathbf{s}}^B_{t_{n+\frac{1}{2}}} \approx \frac{\mathbf{s}^B_{t_{n+1}} - \mathbf{s}^B_{t_n}}{\Delta t}. \tag{40}$$

For the time derivative of the momentum, the inertia forces acing on the two connected nodes, respectively, follows

$$\dot{\mathbf{l}}(\mathbf{s}_{t_{n+\frac{1}{2}}}) = \mathbf{M}_{\text{ce}} \dot{\mathbf{s}}^{AB}_{t_{n+\frac{1}{2}}} = \mathbf{M}_{\text{ce}} \begin{bmatrix} \dot{\mathbf{s}}^A_{t_{n+\frac{1}{2}}} \\ \dot{\mathbf{s}}^B_{t_{n+\frac{1}{2}}} \end{bmatrix}. \tag{41}$$

The mixed formulation and the use of the velocity in the inertia term make it necessary to establish the linear equilibrium of momentum to ensure that $\dot{\mathbf{q}} = \mathbf{s}$ at any time instant.

$$\mathbf{l}(\mathbf{q}) - \mathbf{l}(\mathbf{s}) = \mathbf{M}_{\text{ce}} \big( \frac{\mathbf{q}^{AB}_{t_{n+1}} - \mathbf{q}^{AB}_{t_n}}{\Delta t} - \frac{\mathbf{s}^{AB}_{t_{n+1}} + \mathbf{s}^{AB}_{t_n}}{2} \big) \tag{42}$$

Analogous to the internal forces due to the elasticity of the coupling element, the inertia forces related to the mass are also linearised. The derivative of $\dot{\mathbf{l}}(\mathbf{s})$ with respect to $\mathbf{q}$ becomes zero.

$$\frac{\partial}{\partial \mathbf{q}^{AB}_{t_{n+1}}} \Big( \mathbf{M}_{\text{ce}} \dot{\mathbf{s}}^{AB}_{t_{n+\frac{1}{2}}} \Big) = 0. \tag{43}$$

Because the term depends on the generalised velocities as the acceleration $\dot{\mathbf{s}}^{AB}_{t_{n+\frac{1}{2}}} \approx \frac{\mathbf{s}^{AB}_{t_{n+1}} - \mathbf{s}^{AB}_{t_n}}{\Delta t}$, linearisation with respect to the generalised velocity is needed. This term reads

$$\mathbf{K}_{qs} = \frac{\partial}{\partial \mathbf{s}^{AB}_{t_{n+1}}} \Big( \mathbf{M}_{\text{ce}} \dot{\mathbf{s}}^{AB}_{t_{n+\frac{1}{2}}} \Big)$$

$$= \frac{\partial}{\partial \mathbf{s}^{AB}_{t_{n+1}}} \Big( \mathbf{M}_{\text{ce}} \Big( \frac{\mathbf{s}^{AB}_{t_{n+1}} - \mathbf{s}^{AB}_{t_n}}{\Delta t} \Big) \Big)$$
$$= \frac{1}{\Delta t} \mathbf{M}_{\text{ce}}. \tag{44}$$

The equivalence of momentum is derived accordingly with respect to $\mathbf{q}$ and $\mathbf{s}$

$$\mathbf{K}_{sq} = \frac{\partial}{\partial \mathbf{q}^{AB}_{t_{n+1}}} \Big( \mathbf{M}_{\text{ce}} \Big( \frac{\mathbf{q}^{AB}_{t_{n+1}} - \mathbf{q}^{AB}_{t_{n+}}}{\Delta t} - \frac{\mathbf{s}^{AB}_{t_{n+1}} + \mathbf{s}^{AB}_{t_n}}{2} \Big) \Big)$$
$$= \frac{1}{\Delta t} \mathbf{M}_{\text{ce}}, \tag{45}$$

$$\mathbf{K}_{ss} = \frac{\partial}{\partial \mathbf{s}^{AB}_{t_{n+1}}} \Big( \mathbf{M}_{\text{ce}} \Big( \frac{\mathbf{q}^{AB}_{t_{n+1}} - \mathbf{q}^{AB}_{t_n}}{\Delta t} - \frac{\mathbf{s}^{AB}_{t_{n+1}} + \mathbf{s}^{AB}_{t_n}}{2} \Big) \Big)$$
$$= -\frac{1}{2} \mathbf{M}_{\text{ce}}. \tag{46}$$

## 3.3 Derivation of the damping forces

It remains to introduce a damping formulation into the coupling element in order to dissipate numerically nonphysical high frequencies and to model physical damping properties of flexible couplings. We chose a damping formalism according to [19, 28]. The formulation chosen in the spatially and temporally discrete governing equation (7) allows the use of first order dissipation functions. Higher order dissipation functions are possible but are beyond the scope of this paper. To demonstrate that different first order dissipation functions can be used, we implement two different dissipation functions. In future work, these dissipation functions can be adapted to other physical problems that need to be addressed, such as specific material damping properties.
The applied stress/strain dependent damping is added as a non-conservative term to the internal forces

$$\mathbf{f}^{\text{int}} = \mathbf{f}^{\text{int}}_{\text{conservative}} + \mathbf{f}^{\text{int}}_{\text{non-conservative}}. \tag{47}$$

### 3.3.1 First order dissipation scheme

The dissipation function proposed by Armero et al. [28] is applied. Gebhardt et al. [19] also developed a similar kind of damping algorithm but followed a derivation strategy based on the *average-vector-field*. They added perturbations to the discretised equation of motion, which lead to conservation or dissipation properties. They proposed both a stress/strain-based damping algorithm and a velocity-based algorithm. In the present work we focus on the stress/strain-based damping forces and moments and in a second step modify the equation to demonstrate the possibility of implementing different dissipation functions using the example of a strain-rate/stress-rate dependent dissipation function.
Without diving into particulars, we refer to the aforementioned literature for the

derivation of the correlation between deformation and damping forces and moments. This formulation maintains the framework's objectivity naturally. The forces and moments are determined as follows

$$\mathbf{F}_{\text{diss}} = \frac{D_\Gamma}{\|\mathbf{\Gamma}_{t_{n+1}} - \mathbf{\Gamma}_{t_n}\|_{\mathbf{C}_\Gamma}} \cdot \frac{\mathbf{C}_\Gamma(\mathbf{\Gamma}_{t_{n+1}} - \mathbf{\Gamma}_{t_n})}{\|\mathbf{\Gamma}_{t_{n+1}} - \mathbf{\Gamma}_{t_n}\|_{\mathbf{C}_\Gamma}}, \tag{48}$$

$$\mathbf{M}_{\text{diss}} = \frac{D_\Omega}{\|\mathbf{\Omega}_{t_{n+1}} - \mathbf{\Omega}_{t_n}\|_{\mathbf{C}_\Omega}} \cdot \frac{\mathbf{C}_\Omega(\mathbf{\Omega}_{t_{n+1}} - \mathbf{\Omega}_{t_n})}{\|\mathbf{\Omega}_{t_{n+1}} - \mathbf{\Omega}_{t_n}\|_{\mathbf{C}_\Omega}}. \tag{49}$$

$\|\dots\|_{\mathbf{C}} = \sqrt{\langle(\dots)^{\mathrm{T}}, \mathbf{C}\cdot(\dots)\rangle}$ denotes the weighted vector norm. $\mathbf{C}_\Gamma$ and $\mathbf{C}_\Omega$ are the elasticity matrices according to the deformations $\mathbf{\Gamma}$ and $\mathbf{\Omega}$, respectively. Analog to the conservative forces and moments, we summarize the the dissipative forces and moments in the vector $\mathbf{N}_{\text{diss}}$

$$\mathbf{N}_{\text{diss}} = \begin{bmatrix} \mathbf{F}_{\text{diss}} \\ \mathbf{M}_{\text{diss}} \end{bmatrix}. \tag{50}$$

It remains to define the scalar dissipation functions $D_\Gamma$ and $D_\Omega$. They are proposed as

$$D_\Gamma = \frac{1}{2}\chi_\Gamma \|\mathbf{\Gamma}_{t_{n+1}} - \mathbf{\Gamma}_{t_n}\|^2_{\mathbf{C}_\Gamma}, \tag{51}$$

$$D_\Omega = \frac{1}{2}\chi_\Omega \|\mathbf{\Omega}_{t_{n+1}} - \mathbf{\Omega}_{t_n}\|^2_{\mathbf{C}_\Omega}. \tag{52}$$

The dimensionless parameters $\chi_\Gamma$ and $\chi_\Omega$ allow to determine the scale of the dissipation forces and moments. They can be adapted by the user according to the model. This leads to the implemented terms for the discrete damping force and moment

$$\mathbf{F}_{\text{diss}} = \frac{1}{2}\chi_\Gamma \mathbf{C}_\Gamma(\mathbf{\Gamma}_{t_{n+1}} - \mathbf{\Gamma}_{t_n}), \tag{53}$$

$$\mathbf{M}_{\text{diss}} = \frac{1}{2}\chi_\Omega \mathbf{C}_\Omega(\mathbf{\Omega}_{t_{n+1}} - \mathbf{\Omega}_{t_n}). \tag{54}$$

### 3.3.2 Modified first order dissipation scheme

We demonstrate in the following that the formulation briefly summarised in section 3.3.1, can encompass various dissipation functions. The parameters $\chi_\Gamma$ and $\chi_\Omega$ can be chosen arbitrarily to adapt the damping magnitude to the specific application. Therefore, it is appropriate to choose $\chi_\Gamma = \frac{\alpha_\Gamma}{\Delta t}$ and $\chi_\Omega = \frac{\alpha_\Omega}{\Delta t}$, which implies that the damping forces and moments are dependent on the deformation rate rather than the absolute deformation. $\alpha_\Gamma$ and $\alpha_\Omega$ are again parametrisation factors without dimension. This inspires the conversion of the numerical derivatives into analytical derivatives of the deformation measure.

$$\mathbf{F}_{\text{diss}} = \lim_{\Delta t \to 0} \frac{1}{2}\alpha_\Gamma \mathbf{C}_\Gamma \frac{\mathbf{\Gamma}_{t_{n+1}} - \mathbf{\Gamma}_{t_n}}{\Delta t} \quad \rightarrow \quad \tilde{\mathbf{F}}_{\text{diss}} = \frac{1}{2}\alpha_\Gamma \mathbf{C}_\Gamma \dot{\mathbf{\Gamma}}_{t_{n+\frac{1}{2}}} \tag{55}$$

$$\mathbf{M}_{\text{diss}} = \lim_{\Delta t \to 0} \frac{1}{2} \alpha_\Omega \mathbf{C}_\Omega \frac{\boldsymbol{\Omega}_{t_{n+1}} - \boldsymbol{\Omega}_{t_n}}{\Delta t} \quad \rightarrow \quad \tilde{\mathbf{M}}_{\text{diss}} = \frac{1}{2} \alpha_\Omega \mathbf{C}_\Omega \dot{\boldsymbol{\Omega}}_{t_{n+\frac{1}{2}}} \tag{56}$$

For the sake of completeness, a scalar dissipation function can also be identified for this in accordance with the derivation from [19]. A minimum dissipative force is sought that satisfies the relationship (analogously for $\boldsymbol{\Omega}$) denoted in equation 58

$$\frac{1}{2} \|\mathbf{F}_{\text{diss}}\|^2_{\mathbf{C}} \quad \rightarrow \quad \min, \tag{57}$$

$$\langle \mathbf{F}_{\text{diss}}, \boldsymbol{\Gamma}_{t_{n+1}} - \boldsymbol{\Gamma}_{t_n} \rangle - \mathcal{D}(\boldsymbol{\Gamma}_{t_{n+1}}, \boldsymbol{\Gamma}_{t_n}) = 0. \tag{58}$$

We modify this derivation so that the dissipation force depends on the deformation rate instead on the absolute deformation

$$\frac{1}{2} \|\mathbf{F}_{\text{diss}}\|^2_{\mathbf{C}} \quad \rightarrow \quad \min, \tag{59}$$

$$\langle \mathbf{F}_{\text{diss}}, \dot{\boldsymbol{\Gamma}}_{t_{n+\frac{1}{2}}} \rangle - \mathcal{D}(\dot{\boldsymbol{\Gamma}}_{t_{n+\frac{1}{2}}}) = 0. \tag{60}$$

Without repeating the derivation this leads to the strain-rate dependent dissipation functions

$$\tilde{\mathcal{D}}_\Gamma = \frac{1}{2} \alpha_{\dot{\Gamma}} \langle \mathbf{C} \dot{\boldsymbol{\Gamma}}_{t_{n+\frac{1}{2}}}, \dot{\boldsymbol{\Gamma}}_{t_{n+\frac{1}{2}}} \rangle, \tag{61}$$

$$\tilde{\mathcal{D}}_\Omega = \frac{1}{2} \alpha_{\dot{\Omega}} \langle \mathbf{C} \dot{\boldsymbol{\Omega}}_{t_{n+\frac{1}{2}}}, \dot{\boldsymbol{\Omega}}_{t_{n+\frac{1}{2}}} \rangle. \tag{62}$$

The analytical time derivative of the deformation measure $\mathbf{u}$ is determined as

$$\dot{\mathbf{u}} = \frac{\partial}{\partial t} \mathbf{u} = \begin{bmatrix} \dot{\boldsymbol{\Gamma}} \\ \dot{\boldsymbol{\Omega}} \end{bmatrix} \tag{63}$$

$$= \frac{1}{2\eta} \begin{bmatrix} \mathbf{x}^B(\dot{\mathbf{d}}_i^A + \dot{\mathbf{d}}_i^B)) + \dot{\mathbf{x}}^B(\mathbf{d}_i^A + \mathbf{d}_i^B)) - \mathbf{x}^A(\dot{\mathbf{d}}_i^A + \dot{\mathbf{d}}_i^B)) - \dot{\mathbf{x}}^A(\mathbf{d}_i^A + \mathbf{d}_i^B) \\ \varepsilon_{ijk}(\dot{\mathbf{d}}_j^A \mathbf{d}_k^B + \dot{\mathbf{d}}_k^B \mathbf{d}_j^A - \dot{\mathbf{d}}_k^A \mathbf{d}_j^B - \dot{\mathbf{d}}_j^B \mathbf{d}_k^A) \end{bmatrix}, \tag{64}$$

with $\varepsilon_{ijk}$, the permutation symbol and $i, j, k = 1, 2, 3$. Again, to maintain the readability we omitted indicating the time instants. The deformation components are evaluated at the mid-point as

$$\mathbf{u} = \mathbf{u}_{t_{n+\frac{1}{2}}} \approx \frac{\mathbf{u}_{t_{n+1}} + \mathbf{u}_{t_n}}{2}, \quad \dot{\mathbf{u}} = \dot{\mathbf{u}}_{t_{n+\frac{1}{2}}} \approx \frac{\dot{\mathbf{u}}_{t_{n+1}} + \dot{\mathbf{u}}_{t_n}}{2}. \tag{65}$$

Note that derivations of objective quantities defined in local coordinate systems may not necessarily be objective. As the selected deformation measure comprises quantities defined in the global coordinate system, their time derivatives are also objective.
The damping forces and moments for the first order dissipation scheme are summarised in a vector

$$\mathbf{N}_{\text{diss}} = \frac{1}{2} \boldsymbol{\chi} \mathbf{C} \mathbf{u} = \frac{1}{2} \boldsymbol{\chi} \mathbf{C} (\mathbf{B}^{\mathrm{T}} \mathbf{q}), \tag{66}$$

with

$$\boldsymbol{\chi} = \begin{bmatrix} \chi_\Gamma \mathbf{I} & 0 \\ 0 & \chi_\Omega \mathbf{I} \end{bmatrix} \in \mathbb{R}^{6\times 6}. \tag{67}$$

$\mathbf{I} \in \mathbb{R}^{3\times 3}$ denotes the identity matrix. For the linearisation follows consequently

$$\mathbf{K}_{\text{int,diss}} = \frac{\partial \mathbf{N}_{\text{diss}}}{\partial \mathbf{q}} = \frac{1}{2}\boldsymbol{\chi}\mathbf{C}\mathbf{B}^{\mathrm{T}}. \tag{68}$$

The same entries in the iteration matrix can be used in the modified first order dissipation scheme for sufficiently small $\Delta t$ as the expressions are equal for $\Delta t \to 0$.

# 4 Applications

In this section some application and benchmark examples are shown to illustrate the behaviour of the coupling element. The nonlinear mechanical model of the in-house multi-physical simulation software DeSiO is used. It is briefly presented in section 2. This framework has lately been developed in the context of wind energy, especially to tackle the nonlinear behaviour of large offshore wind turbines.
In section 4.1 a check of the coupling elements formulation's plausibility is shown. In section 4.2 we illustrate the geometrically exact behaviour, a verification against ABAQUS for small displacements as well as a numerical indication of path-independence. Since no geometrically exact spring elements can be used in ABAQUS, we verify the static behaviour of the coupling element on small displacements. Here, linear (ABAQUS) and non-linear (coupling element) deformation measure show the same load-deformation behaviour. A transient and modal analysis is presented in section 4.3 to illustrate the dissipation of high frequencies and the reduction of the total energy. Finally, in section 4.4, we qualitatively demonstrate how the coupling element can be used to model the soil-structure interaction of a wind turbine. We show the influence of the flexible support on the natural frequencies of the complex structure.

## 4.1 Plausibility check of the coupling element formulation in a transient analysis

The deformation measure of the coupling element is based on the Green-Lagrange strain tensor given in equation 5. As shown in equations 17 and 18 the strain tensor can be parameterised by the choice of $\eta$. To proof that the formulations is transferable to the geometrically exact beam, we use this parameter to obtain an equivalent formulation. Furthermore, we model an exemplary application with the coupling element or the geometrically exact beam.
The parameter is $\eta = 1$ m for the coupling element. To obtain the geometrically exact beam formulation, we need to choose $\eta = l$, where $l$ is the length of the beam element, i.e. the distance between the connected nodes resulting from the FE discretisation. The resulting modification of the nonlinear governing equation is taken into account

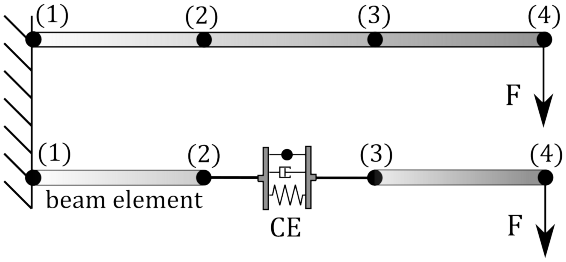


**Fig. 2** Beam/coupling element configuration to compare the resulting iteration matrix

in the iteration matrix as follows:

$$\mathbf{K}_{qq} = \frac{1}{2}\left(\mathbf{K}_1 + \mathbf{K}_2 + \mathbf{K}_m\right) \quad \rightarrow \quad \mathbf{K}_{qq,\mathrm{mod}} = j \cdot w \cdot \mathbf{K}_{qq}, \tag{69}$$

with the Jacobian $j = l/2$ and the weight $w = 2$, resulting from the Gaussian-quadrature as part of the FE formulation. Again, we refer to the description of the geometricaly exact beam theory in the literature, e.g., [27].
The example is schematically illustrated in figure 2. As a benchmark example we chose a horizontally orientated geometrically exact beam, with a length $L = 3.0$ m. The beam is discretised into three elements, with $l = 1.0$ m, using four nodes (1) to (4). The cross-section properties of the beam are equal to a steel beam with a rectangular geometry ($0.02$ m $\times\, 0.02$ m), with a mass density $\rho_{steel} = 7580 \frac{\mathrm{kg}}{\mathrm{m}^3}$, a Young's modulus $\mathrm{E}_{steel} = 210$ MPa and a Poisson's ratio $\nu_{steel} = 0.3$. Node (1) of the beam is clamped. A vertical force of $F = 50.0$ kN is applied to the tip of the beam, node (4). The force is linearly increased within in the time interval $t = [0.0, 2.0]$ s.
In a second model, the beam element between nodes (2) and (3) is removed. Instead, the coupling element replaces the geometrically exact beam element. It is parameterised $\eta = l$ as described above to obtain the exact same formulation as the beam element. The material parameters are the same as for the beam element. The loading scenario is also identical. To compare the formulations, a transient analysis of the systems is performed. The total simulation time is $T = 5.0$ s with a time step size of $\Delta t = 1.0 \cdot 10^{-2}$ s. Since the linearly applied forces are removed after $t = 2.0$ s, the systems can oscillate freely. The following boundary and constraint conditions were applied: the clamping of node (1) is realised by preventing all displacements and rotations of the node. An internal constraint is used for each node (2), (3) and (4). This ensures that the directors remain an orthonormal basis with constant length. No internal constraint is required for node (1), since the prevention of rotations and displacements is redundant.
As the formulations of the beam element and the coupling element are aligned through the parameterisation of the deformation measure of the coupling element, we expect that the iteration matrices are also identical when solving the nonlinear governing equations. Figure 3 shows the iteration matrix for the system consisting of geometrically exact beam elements exclusively 3 (a) and the system where a beam element has

been replaced by the coupling element 3 (b) of time step 500, corresponding to the last simulated time step at $T = 5$ s. In figure 3 (a) and 3 (b), each dot represents a non-zero entry in the respective iteration matrix. The value is indicated by its colour. Labels are added to the matrices to indicate which terms are contained within the fields bounded by the dotted lines. Additionally, coloured squares are drawn within these fields. The orange fields indicate that the entries originate from the beam formulation. The blue squares in figure 3 (b) indicate which fields are derived from the coupling element formulation. Terms from the boundary and constraint conditions are marked in yellow. The entries labelled "I" arise from the boundary condition that provides fixed support. Entries labelled "II" are the result of the internal constraints. Of course, the chosen beam/coupling element formulation does not affect the boundary and constraint conditions of the model.

As the visual comparison of the two matrices suggests, the values are identical. This

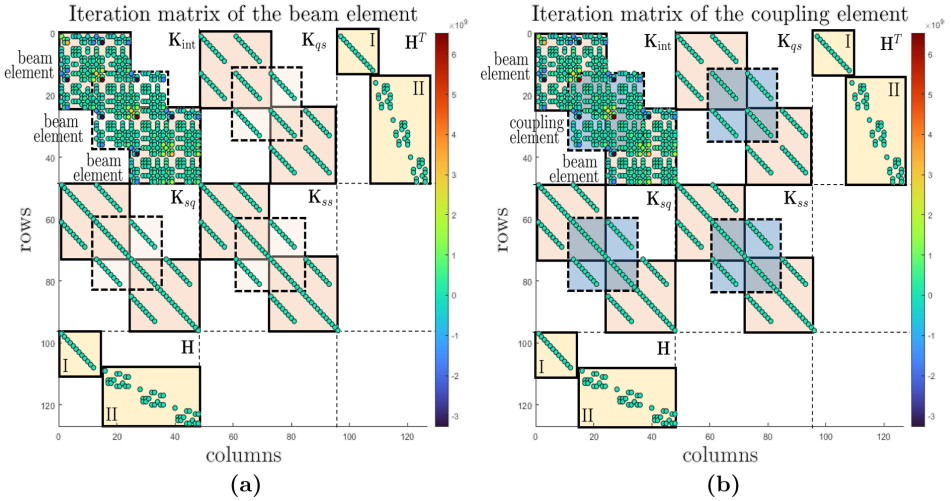


**Fig. 3 (a)** Iteration matrix for $n_{el} = 3$ beam elements at time $T = 5.0$ s, orange: terms related to beam elements, yellow: terms related to boundary and constraint conditions; **(b)** Iteration matrix for $n_{el} = 2$ beam elements + $n_{ce} = 1$ coupling element at time $T = 5.0$ s, orange: terms related to beam elements, blue: terms related to the coupling element, yellow: terms related to boundary and constraint conditions

demonstrates that the formulation of the coupling element can be transformed into the formulation of the geometrically exact beam. Furthermore, this example serves as a plausibility check to ensure the correctness of the implementation.

## 4.2 Static analyses

The coupling element employs a nonlinear deformation measure with geometrically exact behaviour. As discussed, it is therefore suited to model large displacements and rotations of a coupling. For small displacements and rotations the geometric nonlinearity can be neglected. Consequently, it is possible to verify the coupling element's behaviour against an implementation of a linear deformation measure if the occurring displacements and rotations remain small. We consider a simple example of a beam, which is flexibly supported by the coupling element. A load at the tip of the beam induces a moment acting on the coupling element. On that example we first show the transition of linear to geometrically nonlinear behaviour in section 4.2.1. In section 4.2.2 we implement the same beam structure in ABAQUS where a set of linear spring elements are used to model the flexible mounting. The ABAQUS model is used to verify the behaviour for small rotations. In 4.2.3 we indicate the path-independence numerically.
The system under consideration is schematically illustrated in figure 4. The beam has

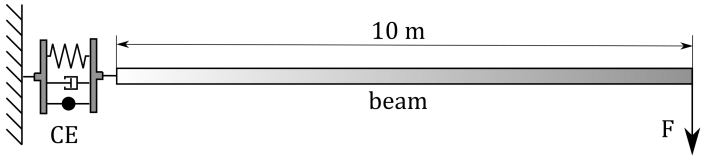


**Fig. 4** Schematic representation of a statically loaded beam, flexibly mounted to the environment

a length of $l = 10$ m. Its cross-section is square with a width of 0.01 m. The material used is steel with $\rho_{steel} = 7580 \frac{\text{kg}}{\text{m}^3}$, $\text{E}_{steel} = 210$ MPa and $\nu_{steel} = 0.3$. The geometrically exact beam is discretised with $n_{el} = 20$ elements. A diagonal elasticity matrix is used for the coupling element ($c_{11} = c_{22} = c_{33} = 2 \cdot 10^6 \frac{\text{N}}{\text{m}}, c_{44} = c_{55} = c_{66} = 5 \cdot 10^4 \frac{\text{Nm}}{\text{rad}}$), see equation 21. The subsequently discussed static analyses without self-weight are performed.

### 4.2.1 Illustration of the geometrically exact mechanical behaviour

To illustrate the geometrically exact behaviour we perform a static analysis with a force $\mathbf{F}$ located at the tip of the beam, see figure 4. The force is applied in increments of $\Delta\mathbf{F} = 0.52$ N per load step. A load step size of $\Delta t = 1.0 \cdot 10^{-3}$ is chosen. The force is increased until a structural problem occurs. Depending on this increasing force, we evaluate the rotation $\phi_{\text{ce}}$ of the node to which the coupling element is attached. The result is plotted in figure 5. The dashed blue straight line $\phi_{lin}$ represents the linear relationship between moment and rotation as would occur with a linear deformation measure. It can be seen that for the given scenario the resulting rotation is approximately the same for small angles up to $\phi \approx 5°$. For larger angles, the geometrically

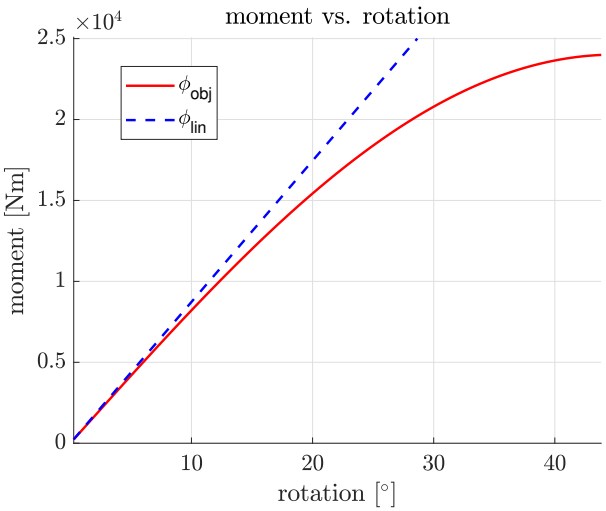


**Fig. 5** Rotation of the coupling element, depending of the moment. Comparison between a linear deformation measure and the implemented objective, geometrically exact deformation measure

exact deformation measure behaves increasingly softer. This behaviour is plausible and physically more exact than the linear relation between rotation and load. The representation allows to perform stability analyses of whole MBS including couplings that are prone to large deformations. In the linear case the stability problem is not visible. In an engineering application this would lead to a more conservative assessment of a component.

### 4.2.2 Verification of the formulation for small deformations

The model illustrated in figure 4 is used to verify the coupling element formulation for small displacements and rotations against commercial software. In section 4.2.1 it is shown that for small rotation angles of the flexible beam a similar behaviour of the geometrically exact and a linear deformation measure can be expected.
We compare the maximum tip deflection of the loaded system against ABAQUS/CAE 2019.HF4 for the fixed and the flexibly supported case. The diagonal elasticity matrix ($c_{11} = c_{22} = c_{33} = 2 \cdot 10^6 \frac{\mathrm{N}}{\mathrm{m}}, c_{44} = c_{55} = c_{66} = 5 \cdot 10^4 \frac{\mathrm{Nm}}{\mathrm{rad}}$) remains unchanged. In ABAQUS, three translational and three rotational spring elements are used with the same elasticity as in the coupling element. ABAQUS applies a linear deformation measure. A simulation time of $T = 2.0$ s was performed with a constant load step of $\Delta\mathbf{F} = 0.15$ N. The maximum force applied to the tip equals $\mathbf{F}_{max} = 300$ N. Self-weight is again not considered. We also determine the results for the fixed case as in ABAQUS no geometrically exact beam is available, instead the nonlinear Timoshenko beam theory is used. By showing that the difference of the tip deflection is small for both clamped beams, we can exclude the beam kinematics as well as the FE discretisation as an influence on the result of the flexibly supported beam. Table 1 contains the results

of both cases. As can be seen here, there are only minor differences, for the clamped

| Support | DeSiO | ABAQUS | Deviation [%] |
|---|---|---|---|
| Fixed [mm] | 57.110 | 57.147 | 0.0647 |
| Rotation angle [°] | - | - | - |
| Flexible [mm] | 658.377 | 656.697 | 0.2558 |
| Rotation angle [°] | 3.4460 | 3.4343 | 0.3407 |

**Table 1**: Comparison of the displacement of the loaded tip of the beam, the rotation of the supporting spring/-coupling element and the relative deviation for rigid and flexible soil; determined with DeSiO and ABAQUS

beam (0.0647 %). The flexible support also shows no significant differences (0.2558 %) for the small rotation of the coupling, and spring elements, respectively. Additionally, table 1 includes the rotation angles of the rotational spring and the coupling element respectively. The rotation of the coupling element is 3.4460°. The rotation is thus within the range of small angles shown in figure 5, where a similar moment/rotation ratio is to be expected.

### 4.2.3 Numerical indication of path-independence

To numerically demonstrate the path-independence of the formulation, again the example described in figure 4 is used. A set of three forces ($F_1 = F_2 = F_3 = 1$ kN) are linearly applied in all three spacial directions simultaneously. The forces are then linearly decreased so that the structure should return to its original position.

Table 2 contains the displacements of the beam tip $u_1$, $u_2$ and $u_3$ depending on the

| **F** [kN] | $u_1$ [m] | $u_2$ [m] | $u_3$ [m] |
|---|---|---|---|
| [0.0 0.0 0.0] | 0.00000000 | 0.00000000 | 0.00000000 |
| [0.2 0.2 0.2] | 0.43966617 | 0.43966617 | -0.01917738 |
| [0.4 0.4 0.4] | 0.88453386 | 0.88453386 | -0.07826113 |
| [0.6 0.6 0.6] | 1.33870986 | 1.33870986 | -0.18050220 |
| [0.8 0.8 0.8] | 1.80751081 | 1.80751081 | -0.33187553 |
| [1.0 1.0 1.0] | 2.29869293 | 2.29869293 | -0.54284693 |
| [0.8 0.8 0.8] | 1.80751081 | 1.80751081 | -0.33187553 |
| [0.6 0.6 0.6] | 1.33870986 | 1.33870986 | -0.18050220 |
| [0.4 0.4 0.4] | 0.88453386 | 0.88453386 | -078261130 |
| [0.2 0.2 0.2] | 0.43966617 | 0.43966617 | -0.01917738 |
| [0.0 0.0 0.0] | 0.00000000 | 0.00000000 | 0.00000000 |

**Table 2**: Displacement of the beam tip, depending on the load path

load. After removing the forces, the calculated deflection is zero again. There is also

no remaining rotation in the coupling element, as this would cause a deflection of the tip, too. This example numerically indicates the path-independence of the formulation. The analytical prove is outside the scope of this paper.

### 4.3 Transient and modal analysis of an oscillating structure

To demonstrate the influence of the coupling element in a transient analysis, we choose a structure that resembles a satellite, as shown in figure 6. The structural parameters are chosen freely on order to model an oscillating system illustrating the dynamic behaviour as well as the influence of the damping. We chose a dissipation parameter $\alpha = 0.5$, that reduces non-physical high frequencies as well as linear and angular momentum, and the total energy of the system. Furthermore, we use a Fast Fourier Transformation (FFT) to show that the low natural frequencies are not affected by the chosen dissipation parameter.

To model the satellite structure, a rigid body is coupled to two geometrically ex-

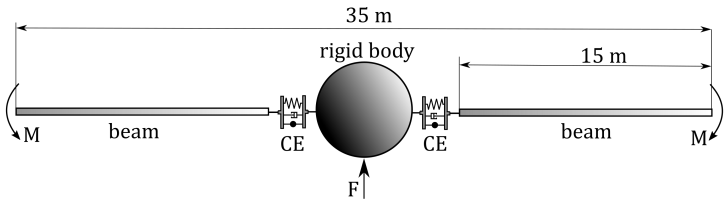


**Fig. 6** Schematic representation of the MBS resembling a satellite structure

act beams. The geometrically exact beams have the properties of a 15.0 m long and 30.0 mm × 30.0 mm wide titanium body ($\rho_{\mathrm{Ti}} = 4500 \frac{\mathrm{kg}}{\mathrm{m}^3}$, $\mathrm{E}_{\mathrm{Ti}} = 120$ MPa, $\nu_{\mathrm{Ti}} = 0.3$). We have chosen a discretisation of $n_{el} = 30$ elements per beam. The properties of the rigid body correspond to an aluminium sphere with $\rho_{\mathrm{Al}} = 2700 \frac{\mathrm{kg}}{\mathrm{m}^3}$ and a radius of $r = 150.0$ mm and thus a mass of $m_{\mathrm{rb}} = 38.88$ kg. It represents the bus of the satellite structure. The properties of the coupling element are chosen such as the connection undergoes significant deformation under the loading of the structure. A diagonal stiffness matrix ($c_{11} = c_{22} = c_{33} = 3 \cdot 10^8 \frac{\mathrm{N}}{\mathrm{m}}, c_{44} = c_{55} = c_{66} = 3 \cdot 10^4 \frac{\mathrm{Nm}}{\mathrm{rad}}$), see equation 21, is applied. For the mass we choose the equivalent of an aluminium sphere with a radius $r_{\mathrm{ce}} = 50.0$ mm, resulting in a weight of $m_{\mathrm{ce}} = 1.414$ kg.

Bending is evoked by applying two moments $M = 500.0$ Nm in opposite directions acting on the tip nodes of the respective beams. The moments are linearly increased over a period of 1.0 s and then abruptly removed, allowing the system to oscillate freely. The oscillatory motion is superposed by a transverse rigid-body motion caused by the force $F = 50.0$ N on the rigid body. It is also increased linearly over the period of 1.0 s and then removed. No gravity has been applied. The total simulation time is $T = 180.0$ s with a constant time step of $\Delta t = 10^{-2}$ s.

In a first scenario, there is no dissipation. Consequently, there are no damping forces and moments to reduce the internal strain energy of the system. In a second scenario, we applied the strain-rate/stress-rate dependent modified first order dissipation

scheme, see section 3.3.1. The dissipation factor $\alpha = \alpha_\Gamma = \alpha_\Omega$ is set to $\alpha = 0.5$, see equations 55 and 56, such that non-physical high frequencies are dissipated. Also, the total energy of the system is reduced without affecting the low natural frequencies. The resulting development of the potential, the kinetic and the total energy of the respective system is shown in figure 8. As no gravity is applied in this example, the potential energy consists only of the internal strain energy, stored in the geometrically exact beams as well as in the coupling elements. The total energy of the system with-

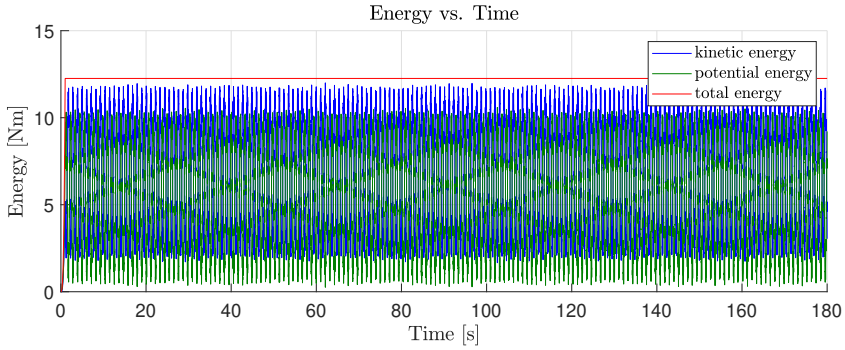


**Fig. 7** Time history of the energy of the satellite structure with dissipation parameter $\alpha = 0.0$

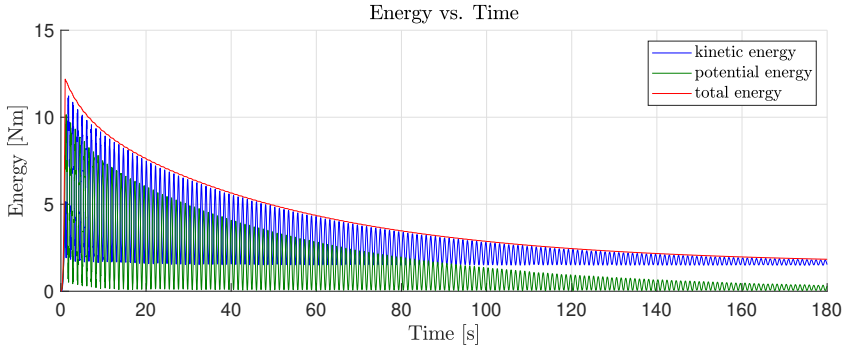


**Fig. 8** Time history of the energy of the satellite structure with dissipation parameter $\alpha = 0.5$

out damping is constant for $t > 1.0$ s due to the presented time integration scheme, see section 2. If damping is employed the total energy is reduced as the flapping movement of the satellite structure diminishes. It tends towards a constant value, which is the result of the rigid body movement caused by the force and elastic energy. The remaining elastic energy is caused by the oscillation of natural frequencies which do not affect the displacement of the coupling element.

The system without damping is subject to vibrations of non-physical high frequencies. Figure 9 (a) shows a zoom into figure 7 in the time interval between 60.0 s and 70.0 s. The comparison of the same time interval in the damped system, shown in figure 9 (b) shows that the high frequency components were dissipated from the oscillation. To prove that the dissipation only reduces the strain energy, we perform

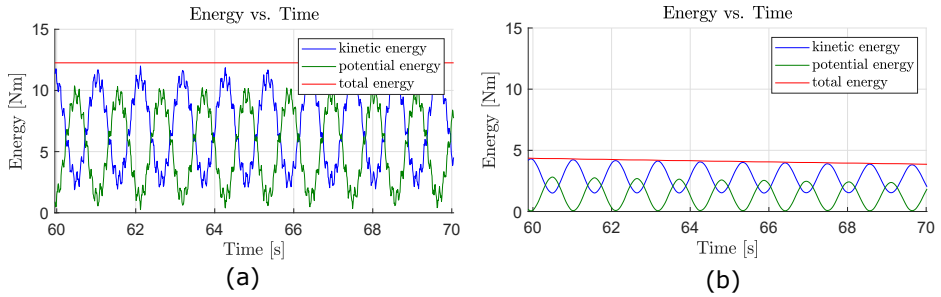


**Fig. 9** Time history of the energy in the interval between 60.0 s and 70.0 s; **(a)** $\alpha = 0.0$, zoom into figure 7; **(b)** $\alpha = 0.5$, zoom into figure 8

another energy analysis after a simulation time of $t = 400.0$ s. In addition, we introduce a small amount strain-dependent damping to the geometrically exact beams, with $\chi = \chi_\Gamma = \chi_\Omega = 0.1$, see equations 48 and 49. This is necessary because some natural frequencies of the oscillating geometrically exact beams do not cause a movement of the coupling element and are therefore not influenced by its damping. Consequently, strain energy would remain. The total energy after the transient analysis of 400.0 s is determined to 1.4585 Nm. This corresponds to the analytically calculated total energy $T$ that is present as kinetic energy due to the rigid body movement. It can be determined with a total mass of the system $m_{total} = 214.808$ kg and a velocity of $v_{satellite} = 0.1163\frac{\mathrm{m}}{\mathrm{s}}$ to $T = \frac{1}{2} m_{total} v_{satellite}^2 = 1.4555$ Nm. This corresponds to a deviation of 0.2057 %.

We chose the dissipation parameter $\alpha = 0.5$. To support this choice, we perform a FFT-analysis for the system with $\alpha = 0$ and with $\alpha = 0.5$ to show that the chosen value has no effect on the low natural frequencies. Still, the total energy of the system is reduced and nonphysical high frequencies are dissipated. Of course, a high dissipation parameter will also affect the lower natural frequencies of a system. To perform the FFT-analysis, we use the same transient simulation data as for the energy conservation illustration above, shown in figure 8. Figure 10 shows the amplitude spectrum resulting from the FFT-analyses. The dampened case $\alpha = 0.5$ is plotted in blue, the system without damping $\alpha = 0.0$ in red. The translational displacements of the beam tip were used as input values for the FFT-analysis. These oscillate in the lower natural frequencies, which are bending natural modes. As mainly the first natural frequency is excited, the first peak at $f = 1.860$Hz, is more pronounced than the following. It is made clear that the chosen dissipation parameter has no influence on the low natural frequencies.

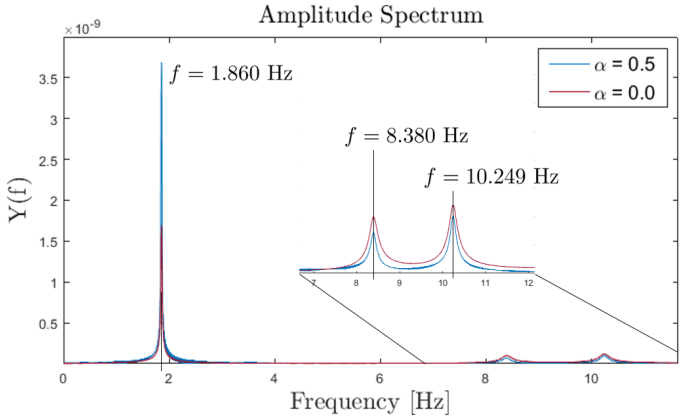


**Fig. 10** FFT-Analyses of the satellite beam displacements, blue $\alpha = 0.5$, red $\alpha = 0.0$

## 4.4 Modal analysis of a wind turbine considering the soil-structure interaction

We use the coupling element to model the soil-structure interaction of a wind turbine to demonstrate its applicability to a complex mechanical example. Furthermore, the influence of the coupling element on the natural frequencies is evaluated qualitatively. In future research we will investigate the soil-structure interaction using the coupling element, including mass and damping.

As the soil-structure interaction can affect the structural behaviour of wind turbine significantly, it is considered in common wind turbine simulation frameworks such as [7–9]. In these simulation tools the complex mechanical behaviour of the surrounding soil can be idealised by a stiffness matrix coupled to the bottom node of the wind turbine tower. To this purpose, we use the coupling element here.

We choose the example of the *IEA-15-240-RWT* reference wind turbine. The geometry, mass and stiffness data are published in the technical report, see [32]. The structure is designed to serve as a benchmark and platform for future wind energy developments. In this example we consider an onshore configuration of the wind turbine, i.e. no substructure is attached below the tower.

In the MBS simulation, the flexible components of the turbine, the blades and the tower, are modelled with geometrically exact beams. The blades and the tower are each spatially discretised with $n_{el} = 40$ elements. Each element of the respective beam is given the corresponding cross-sectional properties published in the technical report. Since the hub and nacelle are not expected to deform significantly, they are idealised by rigid bodies. In the model considered, the blades are mounted with a pitch angle of $\varphi_{pitch} = 0°$. To illustrate the concept, we choose a stiffness matrix with the entries denoted in table 3. These are realistic values chosen according to the methodology described by Häfele et al. [33]. In table 4 we compare the first natural frequencies of the wind turbine structure, both considering rigid and flexible soil. An illustration of the structure is shown in figure 11. Here, the mode shapes corresponding to natural frequencies, in which a tower bending is involved, are shown. The director triads in each

| $c_{11}, c_{22}[\frac{\mathrm{N}}{\mathrm{m}}]$ | $c_{33}[\frac{\mathrm{N}}{\mathrm{m}}]$ | $c_{44}, c_{55}, c_{66}[\frac{\mathrm{Nm}}{\mathrm{rad}}]$ | $c_{15}, c_{51}[\frac{\mathrm{N}}{\mathrm{rad}}]$ | $c_{24}, c_{42}[\frac{\mathrm{N}}{\mathrm{rad}}]$ |
|---|---|---|---|---|
| $2 \cdot 10^9$ | $9 \cdot 10^9$ | $3.0 \cdot 10^{11}$ | $-4 \cdot 10^9$ | $4 \cdot 10^9$ |

**Table 3**: Entries in the elasticity matrix of the coupling element to consider the soil stiffness of a wind turbine foundation

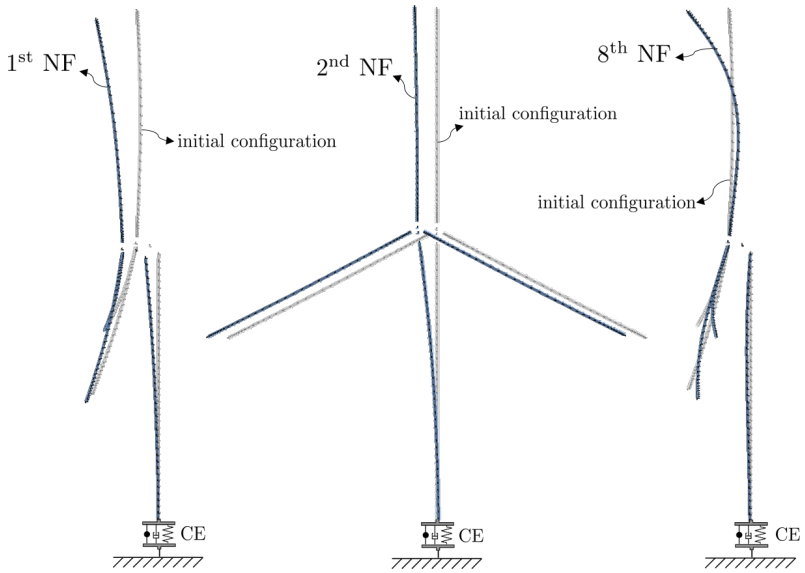


**Fig. 11** Visualisation of the 1st (left), 2nd (centre) and 8th (right) natural frequency (NF) considering the flexibly modelled soil

node can be seen as black dots. The non-deformed initial configuration of the structure is shown in grey, the mode shapes are shown in blue. In table 4 it becomes clear that the flexible coupling of the structure leads to a reduction of the natural frequencies. In particular, a large deviation can be seen in the low natural frequencies (1st NF:

| **NF** [Hz] | 1 | 2 | 3 | 4 | 5 | 6 | 7 | 8 |
|---|---|---|---|---|---|---|---|---|
| **Rigid** | 0.2161 | 0.2189 | 0.5675 | 0.6447 | 0.6973 | 0.9201 | 0.9338 | 1.5180 |
| **Flexible** | 0.2003 | 0.2025 | 0.5648 | 0.6403 | 0.6963 | 0.9191 | 0.9326 | 1.4321 |
| **Deviation** [%] | 7.3398 | 7.5187 | 0.4756 | 0.6878 | 0.1541 | 0.1182 | 0.1237 | 5.6724 |

**Table 4**: Comparison of the first natural frequencies (NF) of the *IEA-15-240-RWT* reference wind turbine for rigid and flexible soil

7.3398%, 2nd NF: 7.5187%). The corresponding natural modes are the bending natural modes of the tower (fore-aft, side-to-side), see figure 11. Therefore, soil deformation is involved and the effect on these frequencies is an expected result. The 8th natural

frequency also involves a higher tower bending natural mode. Thus, again a high deviation regarding the rigid soil can be seen (5.6724%).
The influence of the flexible soil is a plausible result and will be investigated in more detail in future work, together with the mass of the soil and its damping properties.

# 5 Concluding remarks

The motivation of this work was to develop a general node-to-node coupling element formulation to consider geometrical nonlinearities when connecting components in MBS simulations. The coupling element is a consistent contribution to the mechanical framework presented in section 2. Its properties of objectivity, path-independence and the preservation of linear and angular momentum as well as the total energy are maintained. The coupling considers elastic, inertia and damping forces.
We described the mechanical derivation, which allows the computation of the elastic forces on the respective nodes based on a $6 \times 6$ elasticity matrix considering an objective deformation measure. Inertia forces are considered as an arbitrarily shaped continuum between the coupled nodes. A fully populated inertia matrix can be considered accordingly. Strain/stress dependent damping was implemented following the work of Armero and Romero [28] and Gebhardt et al. [19]. In addition, a modification of this formulation has been shown to result in strain-rate/stress-rate dependent damping, demonstrating that different dissipation functions can be used. This allows the damping to be applied to specific physical problems, e.g. considering damping functions that are material dependent.
Finally, we demonstrated the behaviour of the coupling element. In static analyses the geometrically exact behaviour was illustrated compared to a linear deformation measure. For small rotation angles the results were successfully verified against commercial software. In a further example path-independence was indicated numerically. The influence of the damping formalism was demonstrated in transient analyses of an oscillating structure. Finally, the coupling element was applied to model the soil-structure interaction of a wind turbine. A plausible influence on the natural frequencies was shown.
In future work we plan to investigate higher order dissipation functions. A promising application domain of the coupling element is the more detailed consideration of soil-structure interaction. In particular, the modelling of the soil damping behaviour using the coupling element will be investigated. Also of interest is the elastic blade-hub connection of wind turbines, which is assumed to be rigid in conventional MBS simulations. In this work we focused on moderate deformations. To also consider large deformations the application of a nonlinear material model is necessary, which will be object of further research.

**Funding.** Funded by the Deutsche Forschungsgemeinschaft (DFG, German Research Foundation), Project Z01, ID 434502799, SFB 1463
C. Gebhardt gratefully acknowledges the support from the European Research Council via the ERC Consolidator Grant “DATA-DRIVEN OFFSHORE” (Action No. 101083157).

**Author contributions.** D.M. did the main research work and wrote the most of the manuscript text. D.S. and C.H. supported the numerical implementation. C.H., C.G.G. and R.R. supported the conceptualisation. All authors revised and improved the manuscript.

## Declarations

**Competing interests** The authors declare no competing interests.

## References


[1] Riso, C., Cesnik, C.E.S.: Geometrically nonlinear effects in wing aeroelastic dynamics at large deflections. Journal of Fluids and Structures **120**, 103897 (2023) https://doi.org/10.1016/j.jfluidstructs.2023.103897 . Accessed 2023-08-10

[2] Rezaei, M.M., Zohoor, H., Haddadpour, H.: Aeroelastic modeling and dynamic analysis of a wind turbine rotor by considering geometric nonlinearities. Journal of Sound and Vibration **432**, 653–679 (2018) https://doi.org/10.1016/j.jsv.2018.06.063 . Accessed 2023-08-10

[3] Andruet, R.H., Dillard, D.A., Holzer, S.M.: Two- and three-dimensional geometrical nonlinear finite elements for analysis of adhesive joints. International Journal of Adhesion and Adhesives **21**(1), 17–34 (2001) https://doi.org/10.1016/S0143-7496(00)00024-5 . Accessed 2023-07-14

[4] Dispersyn, J., Santarsiero, M., Belis, J., Louter, C.: A preliminary study of the nonlinearity of adhesive point-fixings in structural glass facades. Journal of Facade Design and Engineering **2**(1-2), 85–107 (2014) https://doi.org/10.3233/FDE-140015 . Accessed 2023-07-14

[5] Apalak, M.K., Apalak, Z.G., Gunes, R.: Thermal and Geometrically Nonlinear Stress Analyses of an Adhesively Bonded Composite Tee Joint with Double Support. Journal of Thermoplastic Composite Materials **17**(2), 103–136 (2004) https://doi.org/10.1177/0892705704033337 . Accessed 2023-07-14

[6] Javořík, J., Kledrowetz, J., Keerthiwansa, R., Nekoksa, P.: The Numerical Analysis of Axially Loaded Elastomeric Bushing. Materials Science Forum **919**, 315–324 (2018) https://doi.org/10.4028/www.scientific.net/MSF.919.315 . Accessed 2023-07-14

[7] Jonkman, J.M., Buhl, M.L.J.: FAST User's Guide - Updated August 2005. Technical Report NREL/TP-500-38230, 15020796 (October 2005). https://doi.org/10.2172/15020796 . http://www.osti.gov/servlets/purl/15020796-vtWXa3/ Accessed 2023-06-14

[8] Kim, T., Hansen, A.M., Branner, K.: Development of an anisotropic beam finite

element for composite wind turbine blades in multibody system. Renewable Energy **59**, 172–183 (2013) https://doi.org/10.1016/j.renene.2013.03.033 . Accessed 2023-01-12

[9] Bossanyi, E.A., Witcher, D., Quarton, D.C.: User Manual GH Bladed 3.51 (2003)

[10] Borri, M., Bottasso, C.L., Trainelli, L.: An invariant-preserving approach to robust finite-element multibody simulation. ZAMM **83**(10), 663–676 (2003) https://doi.org/10.1002/zamm.200310065 . Accessed 2023-08-22

[11] Betsch, P., Steinmann, P.: Frame-indifferent beam finite elements based upon the geometrically exact beam theory. International Journal for Numerical Methods in Engineering **54**(12), 1775–1788 (2002) https://doi.org/10.1002/nme.487 . Accessed 2022-05-19

[12] Romero, I., Armero, F.: An objective finite element approximation of the kinematics of geometrically exact rods and its use in the formulation of an energy–momentum conserving scheme in dynamics. International Journal for Numerical Methods in Engineering **54**(12), 1683–1716 (2002) https://doi.org/10.1002/nme.486 . Accessed 2023-01-05

[13] Gebhardt, C.G.: Desarrollo de simulaciones numéricas del comportamiento aeroelástico de grandes turbinas eólicas de eje horizontal. PhD thesis (2012)

[14] Gebhardt, C.G., Hofmeister, B., Hente, C., Rolfes, R.: Nonlinear dynamics of slender structures: a new object-oriented framework. Computational Mechanics **63**(2), 219–252 (2019) https://doi.org/10.1007/s00466-018-1592-7 . Accessed 2022-02-22

[15] Gebhardt, C.G., Rolfes, R.: On the nonlinear dynamics of shell structures: Combining a mixed finite element formulation and a robust integration scheme. Thin-Walled Structures **118**, 56–72 (2017) https://doi.org/10.1016/j.tws.2017.05.001 . Accessed 2022-02-22

[16] Gebhardt, C.G., Steinbach, M.C., Rolfes, R.: Understanding the nonlinear dynamics of beam structures: A principal geodesic analysis approach. Thin-Walled Structures **140**, 357–372 (2019) https://doi.org/10.1016/j.tws.2019.03.009 . Accessed 2022-02-22

[17] Gebhardt, C.G.: Robust computational procedures for the nonlinear dynamic analysis of beam and shell structures (2020) https://doi.org/10.15488/9790 . Publisher: Hannover : Institut für Statik und Dynamik, Leibniz Universität Hannover. Accessed 2023-08-10

[18] Hente, C., Gebhardt, C.G., Pache, D., Rolfes, R.: On the modal analysis of nonlinear beam and shell structures with singular mass and stiffness matrices. Thin-Walled Structures **144**, 106310 (2019) https://doi.org/10.1016/j.tws.2019.

106310 . Accessed 2023-08-11

[19] Gebhardt, C.G., Romero, I., Rolfes, R.: A new conservative/dissipative time integration scheme for nonlinear mechanical systems. Computational Mechanics **65**(2), 405–427 (2020) https://doi.org/10.1007/s00466-019-01775-3 . Accessed 2022-02-22

[20] Hente, C., Gebhardt, C.G., Rolfes, R.: On the static analysis of nonlinear beam and shell structures with singular stiffness matrices due to redundant coordinates. Thin-Walled Structures **161**, 107496 (2021) https://doi.org/10.1016/j.tws.2021.107496 . Accessed 2023-07-18

[21] Abaqus Theory Manual. Abaqus Version 6.7 edition (2023)

[22] Adams View User's Guide. Adams 2021.3 (2023)

[23] Masarati, P., Morandini, M.: Intrinsic deformable joints. Multibody System Dynamics **23**(4), 361–386 (2010) https://doi.org/10.1007/s11044-010-9194-y . Accessed 2023-02-02

[24] Bauchau, O.A.: Flexible Multibody Dynamics. Solid Mechanics and Its Applications, vol. 176. Springer, Dordrecht (2011). https://doi.org/10.1007/978-94-007-0335-3 . https://link.springer.com/10.1007/978-94-007-0335-3 Accessed 2023-06-20

[25] Armero, F., Romero, I.: On the formulation of high-frequency dissipative time-stepping algorithms for nonlinear dynamics. Part II: second-order methods. Computer Methods in Applied Mechanics and Engineering **190**(51), 6783–6824 (2001) https://doi.org/10.1016/S0045-7825(01)00233-X . Accessed 2022-02-22

[26] Simo, J.C.: A finite strain beam formulation. The three-dimensional dynamic problem. Part I. Computer Methods in Applied Mechanics and Engineering **49**(1), 55–70 (1985) https://doi.org/10.1016/0045-7825(85)90050-7 . Accessed 2023-01-04

[27] Géradin, M., Cardona, A.: Flexible Multibody Dynamics: a Finite Element Approach. John Wiley, New York (2001)

[28] Armero, F., Romero, I.: Energy-dissipative momentum-conserving time-stepping algorithms for the dynamics of nonlinear Cosserat rods. Computational Mechanics **31**(1-2), 3–26 (2003) https://doi.org/10.1007/s00466-002-0389-9 . Accessed 2022-11-08

[29] Nocedal, J., Wright, S.J.: Numerical Optimization, 2nd ed edn. Springer series in operations research. Springer, New York (2006). OCLC: ocm68629100

[30] Betsch, P., Steinmann, P.: Constrained dynamics of geometrically exact

beams. Computational Mechanics **31**(1), 49–59 (2003) https://doi.org/10.1007/s00466-002-0392-1 . Accessed 2023-01-05

[31] Gebhardt, C.G., Steinbach, M.C., Schillinger, D., Rolfes, R.: A Framework for Data-Driven Computational Dynamics Based on Nonlinear Optimization (arXiv:1912.11391) (2019). arXiv:1912.11391 [cs, math] type: article. Accessed 2022-11-08

[32] Gaertner, E., Rinker, J., Sethuraman, L., Zahle, F., Anderson, B., Barter, G., Abbas, N., Meng, F., Bortolotti, P., Skrzypinski, W., Scott, G., Feil, R., Bredmose, H., Dykes, K., Shields, M., Allen, C., Viselli, A.: IEA Wind TCP Task 37: Definition of the IEA 15-Megawatt Offshore Reference Wind Turbine. Technical Report NREL/TP–5000-75698, 1603478 (March 2020). https://doi.org/10.2172/1603478 . https://www.osti.gov/servlets/purl/1603478/ Accessed 2023-06-12

[33] Häfele, J., Huebler, C., Gebhardt, C.G., Rolfes, R.: An improved two-step soil-structure interaction modeling method for dynamical analyses of offshore wind turbines. Applied Ocean Research **55**, 141–150 (2016) https://doi.org/10.1016/j.apor.2015.12.001